

# Impact of Atrial Fibrillation on Left Atrium Haemodynamics: A Computational Fluid Dynamics Study

Mattia Corti<sup>a</sup>, Alberto Zingaro<sup>a</sup>, Luca Dede<sup>a</sup>, Alfio Maria Quarteroni<sup>a,b</sup>

<sup>a</sup>*MOX-Dipartimento di Matematica, Politecnico di Milano, Piazza Leonardo da Vinci 32, Milan, 20133, Italy*

<sup>b</sup>*Chair of Modelling and Scientific Computing (CMCS), Institute of Mathematics, École Polytechnique Fédérale de Lausanne, Station 8, Av. Piccard, Lausanne, CH-1015, Switzerland (Professor Emeritus)*

---

## Abstract

We analyze left atrium haemodynamics, highlighting differences among healthy individuals and patients affected by atrial fibrillation. The computational study is based on patient-specific geometries of the left atria to simulate blood flow dynamics. We devise a novel procedure aimed at recovering the boundary conditions for the 3D haemodynamics simulations, particularly useful in absence of specific ones provided by clinical measurements. With this aim, we introduce a parametric definition of the atria displacement, and we employ a closed-loop lumped parameter model of the whole cardiocirculatory system conveniently tuned on the basis of the patient characteristics. We evaluate a number of fluid dynamics indicators for the atrial haemodynamics, validating our numerical results in terms of several clinical measurements; we investigate the impact of geometrical and clinical features on the risk of thrombosis. To analyse the correlation of thrombus formation with atrial fibrillation, coherently with the medical evidence, we propose a novel indicator, which we call age stasis and that arises from the combination of Eulerian and Lagrangian quantities. This indicator identifies regions where the slow flow cannot rinse the chamber properly, accumulating stale blood particles and creating optimal conditions for clot formation.

*Keywords:* Computational Fluid Dynamics, Cardiac Modeling, Left Atrium Haemodynamics, Atrial Fibrillation, Left Atrial Appendage

---

## 1. Introduction

Nowadays, atrial fibrillation (AF) is the most common cardiac electric dysfunction worldwide [1]. The irregular electrical impulses characterizing this pathology cause a reduced atrial contraction and thus blood ejection. According to the European Society of Cardiology (ESC), in 2016, 7.6 million people aged 65 and over were affected by AF in the European Union. Figures are predicted to increase up to 14.4 million within 2060 [1].

In terms of pathology severity, AF can be classified into three categories: paroxysmal AF is an episode that typically self-terminates within seven days; persistent AF requires termination by pharmacological or direct-current electric cardioversion, and; permanent AF is irreversible to

---

*Email address:* [mattia.corti@polimi.it](mailto:mattia.corti@polimi.it) (Mattia Corti)

sinus rhythm [2, 3, 4]. The persistence of AF may cause remodelling of the atrial chambers on the long term, producing an increase of the atrial volume and possible thrombogenic formation in the Left Atrial Appendage (LAA) [5, 6].

In this paper, we investigate the effects of AF on instantaneous cardiac haemodynamics. Cardiac blood flow analysis is commonly assessed via both imaging and experimental techniques. For instance, 4D flow MRI [7], one of the most advanced imaging techniques, allows the detection of a time-dependent blood flow field [8], the estimate of haemodynamics parameters as flow stasis, mean velocity [9], and particle tracking [10]. However, the resolution provided by 4D flow MRI might be not enough to accurately catch the complexity of cardiac flows and their transitional effects: formation of shear layers, small vortices, and their interactions [11, 12, 13, 14, 15]. For this reason, in-silico simulations of the heart, often combined with medical images, stand as a valuable tool for a more accurate description of blood flows and to estimate a number of haemodynamic indicators as the wall shear stress (WSS) [16, 17, 18, 19].

Literature abounds with CFD studies of human atria under AF, both for idealized [20, 21] and patient-specific geometries [22, 23, 24, 25, 26]. Concerning the numerical approach, in [23], CFD simulations were performed without the application of a turbulence model; in [24, 25], the LA haemodynamics is modeled via the Navier-Stokes (NS) equations in Arbitrary Lagrangian-Eulerian (ALE) formulation; the Variational Multiscale Large Eddy Simulation (VMS-LES) method [27] is considered to model the transitional flow. In [18], a comparison is made considering the differences deriving from applying or not an LES model in AF conditions; the results suggest that, also with a mesh that hasn't the fineness required for DNS, the absence of a turbulence model is acceptable in AF simulations. Due to the relevance of LAA in thrombus formation, many studies analysed how the geometrical morphology of this region of the LA affects the blood flow [28, 29, 30, 31, 32, 33]. These works suggest the existence of a strong correlation between LAA morphology and thromboembolic risk; moreover, AF aggravates this danger.

In this paper, we consider patient-specific geometries of the LA and we carry out CFD simulations providing a full characterization of blood flow in both physiological and pathological conditions. In particular, the atrial geometries we have at our disposal [34, 35] are scanned at the time of end of diastole only [36]. Thus, we are not able to derive from imaging any information about pressures, flows and displacement of the LA [37]. This work proposes first a procedure to overcome the absence of that medical information and to detect meaningful boundary conditions for the CFD simulations, starting from the simulation of a lumped-parameters 0D model [38], in order to use a "one-way" 0D-3D coupling scheme between the circulation and the 3D CFD problem. The circulatory system model is adapted starting from the consideration from [39] to simulate also AF conditions. Contextually, we further tune additional parameters of the model to account for the volumetric constraints given by the patient-specific LA geometries and to obtain meaningful Left Atrial Ejection Fractions (LAEF).

Similarly to what done in [40, 41, 42, 43, 44, 45, 46, 47, 48], we use a parametric displacement combined with patient-specific geometry to fill the lack of information on the chamber displacement. Starting from the analytical formulation in [40], we modify the displacement to catch a more realistic movement of LAA and matching the variations of volume with the physiological or pathological values of the Left Atrial Appendage Ejection Fraction (LAAEF) [49]. We generate a displacement which embodies medical constraints to get a more physiological movement for the chamber and the LAA. We believe this is essential in order to estimate the thrombosis risk in the LA. Moreover, a parametric displacement gives us the possibility to simulate different levels of severity of AF according to the clinical situation of the patients, by conveniently changing the parameters involved in the displacement definition.

In many of the works regarding atrial haemodynamics simulations, the effects of the mitral valve (MV) is mimicked by means of switching boundary conditions [24, 25, 21, 23]. Differently, in this paper we model the effect of the MV on the fluid flow by means of the Resistive Immersed Implicit Surface (RIIS) method [50]. In addition, we prescribe opening and closing times of the valves that are consistent with clinical findings, overcoming the classical over simplification of an instantaneous switch of the valvular status [24, 25, 21, 23]. To the best of our knowledge, the only work in literature which simulates the left atrial haemodynamics considering also the presence of a MV is [51], where a fluid-structure interaction model is employed in order to perform an advanced analysis on the valvular movement.

Finally, we validate our numerical results in terms of several biomarkers from medical literature and we perform an analysis of haemodynamic indicators, both from an Eulerian perspective, deriving them directly from the results of the NS simulation, and a Lagrangian one, in which we obtain the indicators starting from the simulation of the motion of red blood cells inside the LA. We consider them like tracers [16], and, by taking advantage of kinetic theory development for particle transport [52], we derive some Eulerian fields about the age and the washout of the blood [53]. Moreover, by combining the Eulerian information of the flow characteristics and the Lagrangian framework in terms of particles history, we introduce a novel haemodynamic indicator, which detects regions with high thrombotic risk, and is used to make a comparison of the effective risk for different patients. Differently from the existing indicators, the new one highlights regions where the flow is stagnant and the blood mean age is high at the same time. Indeed, these the coexistence of these two situations denotes an high risk of formation of a blood clot. Moreover, we derive a dimensionless indicator, which estimates the percentage of volume associated to a higher risk, and we explore its correlation with the AF pathology.

This paper is organized as follows: we present the mathematical models and methods we use for the haemodynamic atrial simulation in Section 2, then, in Section 3, we introduce our novel procedure to construct the boundary conditions. In Section 4, we recall the numerical simulation setup and we present the cases we analyse. Then, we perform the analysis of Eulerian and Lagrangian indicators in Sections 5.1 and 5.2, respectively. In Section 5.3, we propose our haemodynamics indicator, and assess it in the analysis of the simulated cases. Eventually, conclusions are drawn in Section 6.

## 2. Mathematical models and numerical methods for left atrial haemodynamics

This section introduces the mathematical model to describe the fluid dynamics in LA. Let  $\Omega_t$  be the fluid domain at a specific time instant  $t > 0$  (in current configuration) and let  $\partial\Omega_t$  be its boundary, for  $0 < t < T$ . In heart chambers, the blood is assumed to behave as Newtonian, incompressible and homogeneous fluid [54, 55, 56]. Under this assumption, the Cauchy's stress tensor is defined as  $\boldsymbol{\sigma}(\mathbf{u}, p) = -p\mathbf{I} + \mu(\nabla\mathbf{u} + (\nabla\mathbf{u})^\top)$ , where  $\mathbf{u} : \Omega_t \times (0, T) \rightarrow \mathbb{R}^3$  is the fluid velocity field,  $p : \Omega_t \times (0, T) \rightarrow \mathbb{R}$  the pressure field and  $\mu$  the dynamic viscosity.

In order to express the NS equations in a moving reference framework, we employ the ALE formulation [57]. Let  $\widehat{\Omega} \subset \mathbb{R}^3$  represent the LA domain in its reference configuration, as displayed in Figure 1. We define the ALE map  $\mathcal{A}_t$ , which associates at each point of the reference configuration  $\widehat{\mathbf{x}} \in \widehat{\Omega}$  the corresponding point in the actual one  $\mathbf{x} \in \Omega_t$ , such that  $\mathcal{A}_t : \widehat{\Omega} \rightarrow \Omega_t$  and  $\mathbf{x} = \mathcal{A}_t = \widehat{\mathbf{x}} + \widehat{\mathbf{d}}(\widehat{\mathbf{x}}, t)$ , being  $\widehat{\mathbf{d}}$  the displacement of the domain with respect to the reference configuration.

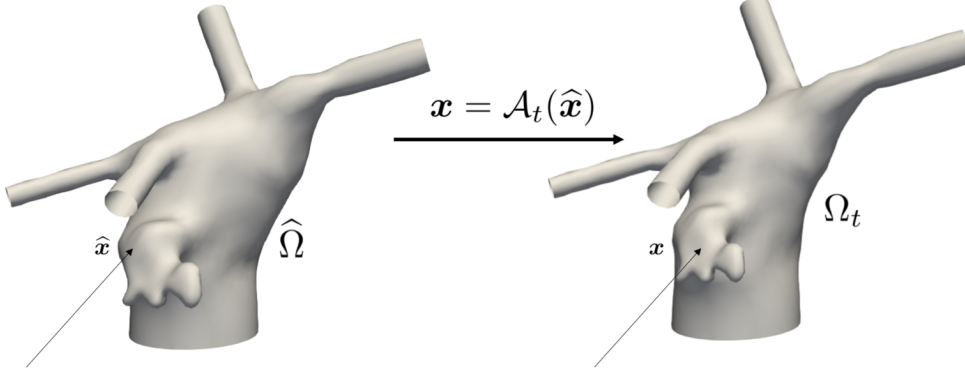


Figure 1: Left atrial domain in reference configuration (left), and current configuration (right), and ALE map  $\mathbf{x} = \mathcal{A}_t(\hat{\mathbf{x}})$ .

As shown in Figure 2, we split the boundary  $\partial\Omega_t$  as:

$$\partial\Omega_t = \Gamma_t^W \cup \Gamma^{\text{MV}} \cup \left( \bigcup_{j=1}^4 \Gamma^{\text{PV}_j} \right), \quad (1)$$

being  $\Gamma_t^W$  the endocardial wall,  $\Gamma^{\text{PV}_j}$  the  $j$ -th pulmonary vein inlet section with  $j = 1, 2, 3, 4$  and  $\Gamma^{\text{MV}}$  the outlet section downstream the MV. For simplicity, we consider the pulmonary veins inlet sections and the outlet section to be fixed. Thus, we neglect the time dependence in the notation.

Should we know a boundary velocity  $\mathbf{g}^{\text{ALE}} : \partial\Omega_t \times (0, T) \rightarrow \mathbb{R}^3$ , we recover the ALE velocity  $\mathbf{u}^{\text{ALE}} : \Omega_t \times (0, T) \rightarrow \mathbb{R}^3$  by means of the following harmonic extension problem:

$$\begin{cases} -\Delta \mathbf{u}^{\text{ALE}} = \mathbf{0} & \text{in } \Omega_t, \\ \mathbf{u}^{\text{ALE}} = \mathbf{g}^{\text{ALE}} & \text{on } \partial\Omega_t, \end{cases} \quad (2)$$

which allows to recover the displacement in any point  $\mathbf{x}$  of the domain  $\Omega_t$  and at any time  $t$  in  $(0, T)$  as:  $\mathbf{d}(\mathbf{x}, t) = \int_0^t \mathbf{u}^{\text{ALE}}(\mathbf{x}, \tau) d\tau$ . Then the NS equations write:

$$\begin{cases} \rho \left( \frac{\partial \mathbf{u}}{\partial t} + ((\mathbf{u} - \mathbf{u}^{\text{ALE}}) \cdot \nabla) \mathbf{u} \right) - \nabla \cdot \boldsymbol{\sigma}(\mathbf{u}, p) + \frac{R}{\varepsilon} \delta_\varepsilon^\Sigma(\varphi)(\mathbf{u} - \mathbf{u}_\Sigma) = \mathbf{0} & \text{in } \Omega_t \times (0, T_{\text{HB}}], \\ \nabla \cdot \mathbf{u} = 0 & \text{in } \Omega_t \times (0, T_{\text{HB}}]. \end{cases} \quad (3)$$

To account for the presence of the MV in the fluid, we use the Resistive Immersed Implicit Surface (RIIS) method, proposed by [50] for the aortic valves simulation, and extended for the ALE case in [17]. With the RIIS method, we identify the MV as an immersed surface described by the level set function  $\varphi : \Omega_t \rightarrow \mathbb{R}$  as  $\Sigma_t^{\text{MV}} = \{\mathbf{x} \in \Omega_t : \varphi(\mathbf{x}) = 0\}$ , and the reaction term is introduced in the momentum balance of NS equation 3. Specifically,  $\varepsilon$  is half-thickness of the MV,  $R$  is the valve resistance, and  $\delta_\varepsilon^\Sigma$  is the smooth Dirac delta function defined as in [50]. The valve velocity is set to be null, using the quasi-static approximation ( $\mathbf{u}_\Sigma = \mathbf{0}$ ) [17].

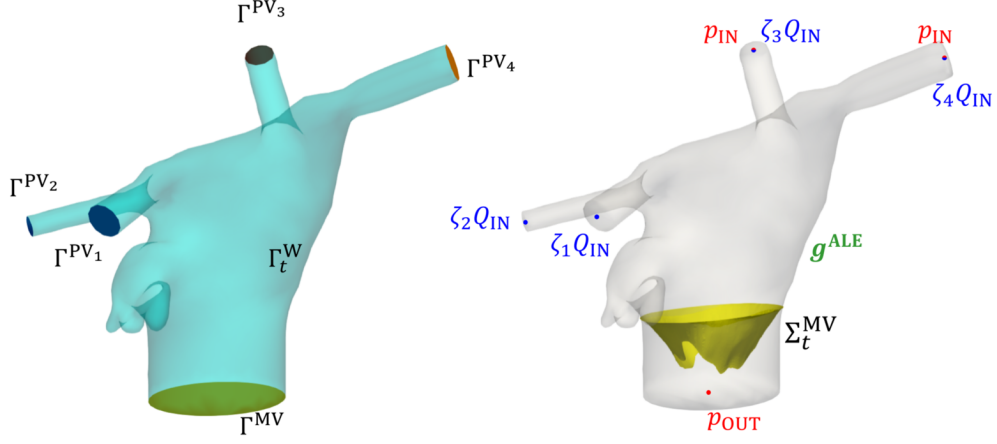


Figure 2: LA domain with details on the boundaries (left), and with the representation of the MV surface  $\Sigma_t^{MV}$  and of the boundary conditions that we prescribed (right).

### 2.1. Boundary and initial conditions

We apply a non-homogeneous Dirichlet no-slip condition  $\mathbf{u} = \mathbf{g}^{ALE}$  on the endocardial wall  $\Gamma_t^W$ ; The boundary data  $\mathbf{g}^{ALE}$  is obtained as presented in Section 3. On the MV section  $\Gamma^{MV}$ , we impose an outflow Neumann boundary condition considering as mean pressure value  $p_{OUT}$ .

Concerning the inlet sections  $\Gamma_j^{PV}$ , we use a Dirichlet boundary condition for all the veins in the diastolic phase  $(0, T_d)$ , imposing an inlet flux  $Q_{IN}$ . However, this is a defective condition [54] and a possible way to fill this gap is to prescribe a parabolic velocity profile to complete the information. In the systolic phase of the heartbeat  $(T_d, T_{HB}]$ , the closure of the MV would not allow a correct estimate of the pressure in the LA without the imposition of a Neumann condition on some of the veins. For this reason, we switch the boundary conditions at two inlet sections, by prescribing the mean pressure value  $p_{IN}$ . In addition, to (weakly) penalize the reverse flow and to avoid numerical instabilities, we introduce backflow stabilization in all the Neumann boundaries [58].

We denote with  $R_j$  the radius of the  $j$ -th inlet section;  $r(\mathbf{x}) = |\mathbf{x}|_2$  is the radial coordinate of the point  $\mathbf{x} \in \Gamma^{PV_j}$ , being  $|\cdot|_2 : \mathbb{R}^3 \rightarrow \mathbb{R}$  the Euclidean norm. To distribute the inlet flowrate in veins having different cross-sections, we introduce  $\zeta_j$  as the flow repartition factor associated to the  $j$ -th vein. In particular, we compute it proportionally to the inlet area as:

$$\zeta_j = \frac{|\Gamma^{PV_j}|}{\sum_{k=1}^4 |\Gamma^{PV_k}|}. \quad (4)$$

The way we compute the boundary conditions  $Q_{IN}$ ,  $p_{IN}$ ,  $p_{OUT}$  and  $\mathbf{g}^{ALE}$  is reported in Section 3.

Moreover, we consider a null initial condition  $\mathbf{u}(\mathbf{x}, 0) = \mathbf{0}$ . The NS-ALE-RIIS equations with the boundary and initial conditions to simulate the LA haemodynamics read:

for every  $t > 0$ , find  $\mathbf{u} : \Omega_t \times (0, T) \rightarrow \mathbb{R}^3$  and  $p : \Omega_t \times (0, T) \rightarrow \mathbb{R}$ :

$$\left\{ \begin{array}{ll} \rho \left( \frac{\widehat{\partial \mathbf{u}}}{\partial t} + ((\mathbf{u} - \mathbf{u}^{\text{ALE}}) \cdot \nabla) \mathbf{u} \right) - \nabla \cdot \boldsymbol{\sigma}(\mathbf{u}, p) + \frac{R}{\varepsilon} \delta_\varepsilon^\Sigma(\varphi) \mathbf{u} = \mathbf{0} & \text{in } \Omega_t \times (0, T_{\text{HB}}], \\ \nabla \cdot \mathbf{u} = 0 & \text{in } \Omega_t \times (0, T_{\text{HB}}], \\ \mathbf{u} = \mathbf{g}^{\text{ALE}} & \text{on } \Gamma_t^{\text{W}} \times (0, T_{\text{HB}}], \\ \mathbf{u} = -2\zeta_k \frac{Q_{\text{IN}}}{|\Gamma^{\text{PV}_k}|} \left( 1 - \frac{r^2}{R_k^2} \right) \mathbf{n}_k & \text{on } \Gamma^{\text{PV}_k} \times (0, T_{\text{HB}}], \\ \mathbf{u} = -2\zeta_j \frac{Q_{\text{IN}}}{|\Gamma^{\text{PV}_j}|} \left( 1 - \frac{r^2}{R_j^2} \right) \mathbf{n}_j & \text{on } \Gamma^{\text{PV}_j} \times (0, T_{\text{d}}], \\ \boldsymbol{\sigma}(\mathbf{u}, p) \mathbf{n}_j = -p_{\text{IN}} \mathbf{n}_j + \rho [(\mathbf{u} - \mathbf{u}^{\text{ALE}}) \cdot \mathbf{n}_j]_- (\mathbf{u} - \mathbf{u}^{\text{ALE}}) & \text{on } \Gamma^{\text{PV}_j} \times (T_{\text{d}}, T_{\text{HB}}], \\ \boldsymbol{\sigma}(\mathbf{u}, p) \mathbf{n} = -p_{\text{OUT}} \mathbf{n} + \rho [(\mathbf{u} - \mathbf{u}^{\text{ALE}}) \cdot \mathbf{n}]_- (\mathbf{u} - \mathbf{u}^{\text{ALE}}) & \text{on } \Gamma^{\text{MV}} \times (0, T_{\text{HB}}], \\ \mathbf{u} = \mathbf{0} & \text{in } \widehat{\Omega}_0 \times \{0\}, \end{array} \right. \quad (5)$$

where  $k = 1, 2$  and  $j = 3, 4$ .

## 2.2. Space and time discretizations

Concerning the numerical approximation of Equation 5, we employ the Finite Element (FE) method for the spatial discretization. We use the VMS-LES method [59, 27] to get a stable formulation of the NS equations discretized with FE (*inf-sup* condition), to stabilize the advection dominated regime, and to account for transitional-nearly turbulent flow regime according to the LES paradigm [40, 44]. Concerning the time discretization, we partition the time domain in  $N_t$  time steps of equal size  $\Delta t$ , and we use the Backward Differentiation Formula (BDF) method of order 1. The treatment of nonlinear terms is semi-implicit with an extrapolation of the velocity field by means of the Newton-Gregory backward polynomials of first order. For more specifics on this method, we refer to [27]. The extension of the VMS-LES method for the NS-ALE-RIIS equations can be found in [41].

Analogously, a FE discretization is used to solve the displacement problem in Equation 2 at each time step.

## 3. Boundary conditions depending on circulation

The medical images we use to carry out the simulations were obtained by [36] and the derived endocardial geometries are openly accessible from the supplementary material of [34, 35]. Since we have static geometries and we do not have additional dynamic images (e.g. cine-MRI), we cannot recover the atrial displacement neither the pressures and fluxes to be prescribed at the boundary. For this reason, we propose a computational procedure aimed at finding these missing data starting from a 0D circulation model and a parametric definition of the boundary displacement. This is a general procedure that can be employed when the data required to carry out CFD simulations are not completely available. We will show in Section 4 that by this procedure we can simulate either physiological and pathological scenarios on the same LA geometry, by simply acting on the 0D circulation model.

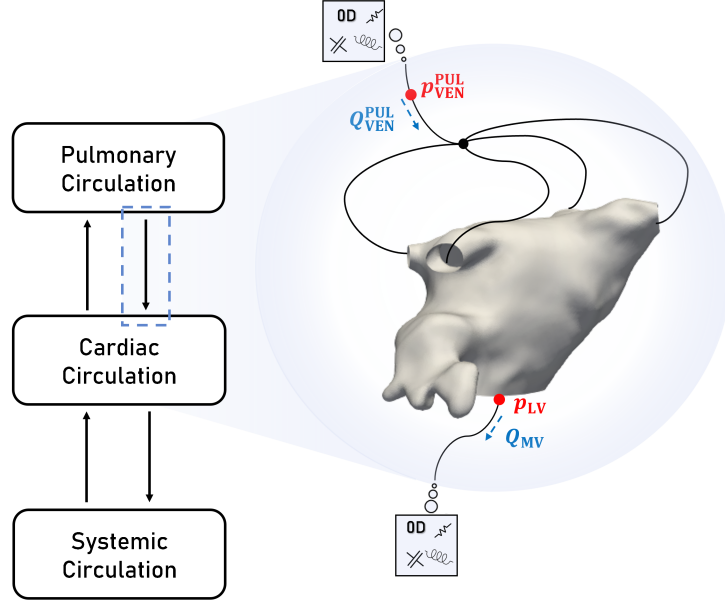


Figure 3: Relation between 0D variables and left atrial domain boundary conditions.

### 3.1. Lumped-parameter model

The mathematical model that we use to derive the boundary conditions is a lumped-parameter model proposed in [38]. It consists of a closed-loop 0D model, where the geometrical reduction allows to represent the complete circulation in a synthetic way, considering only time-dependent variables such as pressures, fluxes and volumes. The model describes the complete cardiovascular system, considering a subdivision in three main compartments: pulmonary, systemic and cardiac circulation. The first two compartments are modeled through RLC circuitual elements, whereas each cardiac chamber is represented by a capacitor with time-varying capacitance, called elastance. The heart valves are modeled via non-ideal diodes.

We use the 0D model to compute integral fluid properties that serve as boundary conditions for the 3D fluid dynamics problem, as shown in Figure 3. The outlet pressure corresponds to the left ventricular one  $p_{OUT} = p_{LV}$ ; the inlet pressure corresponds to the pulmonary veins pressure  $p_{IN} = p_{VEN}^{PUL}$ . Concerning the Dirichlet inlet condition, we use the pulmonary veins flow rate  $Q_{IN} = Q_{VEN}^{PUL}$ . We first carry out a fully 0D simulation, then we use the pressure and flowrates transient to set the boundary conditions to the 3D CFD problem. Our approach can be regarded as a geometric multiscale problem, solved via a splitting algorithm [60].

The lumped-parameter model provides as output the volume of LA  $V_{LA}^{0D}$ , which is used to calibrate the displacement model, as we discuss in Section 3.3.

### 3.2. Accounting for AF in the lumped-parameter circulation model

The model in [38] is tuned to model a healthy individual; for this reason, we need to calibrate the parameters of the 0D model to simulate the AF pathology correctly. To the best of our

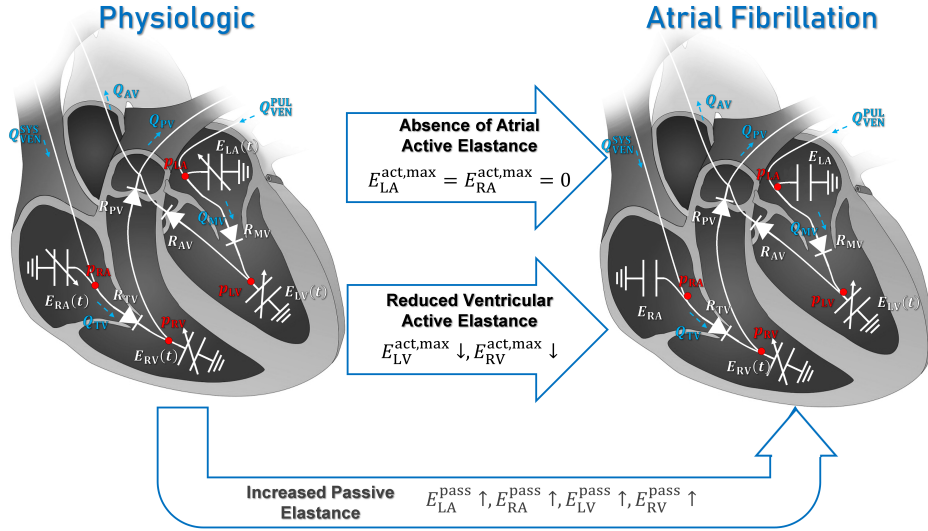


Figure 4: 0D Lumped Parameter Model changes to simulate an AF pathology, with the two corrections (increased passive elastance and reduced  $E_{RV}^{act,max}$ ) necessarily to fit the 3D patient-specific volumes.

knowledge, the only existing work in which a lumped-parameter model is used to simulate the AF pathology is [39]. The variations we use in this work are resumed in Figure 4. We underline that the ones applied to the passive elastances and the right ventricle active elastance are introduced by us to fit the correct 3D volumes of the real patients, while all the others are presented in [39].

The model introduced in [38] defines some time-dependent elastances to simulate the elastic movement of the cardiac muscle, whose analytical formulation is:

$$E_j(t) = \begin{cases} E_j^{pass} + \frac{E_j^{act,max}}{2} \left( 1 - \cos\left(\pi \frac{t}{T_d}\right) \right) & 0 < t \leq T_d, \\ E_j^{pass} + \frac{E_j^{act,max}}{2} \left( 1 + \cos\left(\pi \frac{t - T_d}{T_{HB} - T_d}\right) \right) & T_d < t \leq T_{HB}. \end{cases} \quad (6)$$

Hence, each elastance can vary in the following prescribed range:

$$E_j(t) \in [E_j^{pass}, E_j^{pass} + E_j^{act,max}], \quad j \in \{RA, LA, RV, LV\}. \quad (7)$$

The effect of AF on the mechanical response of the cardiac tissue can be modelled by taking the active elastance equal to zero for both the atria, simulating hence the absence of the ‘‘atrial kick’’ [2, 4], i.e.  $E_{LA}^{act,max} = E_{RA}^{act,max} = 0$ . In AF, this choice implies a constant value for the elastances of the two chambers, namely:

$$E_{LA}(t) = E_{LA}^{pass}, \quad E_{RA}(t) = E_{RA}^{pass} \quad \forall t \in (0, T). \quad (8)$$

Under the pathologic transmission of the electric signal, we model the loss of ventricular contractility, by reducing the active component of the elastances in ventricles.



To simulate the AF geometries, we increase the passive elastances of both atria and ventricles. This choice is fundamental to match the correct volumes and the pulmonary veins pressure. Indeed, the pulmonary hypertension has connection with the AF [61, 62, 63], but without these corrections the pressure values would become even larger than the pathological ones. After our calibration, the model computes also smaller values for the left ventricular pressure  $p_{LV}$  than in physiologic conditions, coherently with the pathological consequences of AF [64, 63].

The passive elastance correction is smaller in atria affected by the remodeling, which caused a volume increase. As a matter of fact, this consequence of the pathology is typically detected by AF lumped-parameter model [39].

### 3.3. Parametrization of the LA wall displacement

Following [41, 40, 44] we assume that the boundary datum  $\mathbf{g}^{\text{ALE}}$ , introduced in Equation 2, can be expressed via separation of variables as:

$$\mathbf{g}^{\text{ALE}}(\mathbf{x}, t) = \mathbf{F}^{\text{ALE}}(\mathbf{x}) h^{\text{ALE}}(t) \quad \text{on } \partial\Omega_t \times (0, T). \quad (9)$$

In the following, we detailed the construction of the two functions  $h^{\text{ALE}}$  and  $\mathbf{F}^{\text{ALE}}$ .

#### 3.3.1. Time-dependent function component

Let  $V_{\text{LA}}(t)$  be the LA volume, then, by using the Reynolds transport theorem (RTT) [65]:

$$\frac{dV_{\text{LA}}}{dt} = \frac{d}{dt} \int_{\Omega_t} d\mathbf{x} \stackrel{\text{(RRT)}}{=} \int_{\partial\Omega_t} \mathbf{g}^{\text{ALE}} \cdot \mathbf{n} d\sigma = h^{\text{ALE}} \int_{\partial\Omega_t} \mathbf{F}^{\text{ALE}} \cdot \mathbf{n} d\sigma, \quad (10)$$

we obtain the following definition of the time-dependent function:

$$h^{\text{ALE}}(t) = \left( \int_{\partial\Omega_t} \mathbf{F}^{\text{ALE}} \cdot \mathbf{n}(t) d\sigma \right)^{-1} \frac{dV_{\text{LA}}(t)}{dt}. \quad (11)$$

Specifically, we set the LA volume to be equal to to the one computed via the 0D circulation model:

$$V_{\text{LA}}(t) = V_{\text{LA}}^{\text{0D}}(t) \quad \forall t \in (0, T). \quad (12)$$

#### 3.4. Space-dependent function and LAA correction

The space-dependent component of the boundary function  $\mathbf{F}^{\text{ALE}}$  is constructed considering two different components on the corresponding reference domain:

$$\widehat{\mathbf{F}}^{\text{ALE}}(\widehat{\mathbf{x}}) = \widehat{\mathbf{f}}^{\text{ALE}}(\widehat{\mathbf{x}}) + \widehat{\mathbf{f}}_{\text{LAA}}^{\text{ALE}}(\widehat{\mathbf{x}}). \quad (13)$$

In Equation 13, we separate the motion of the whole chamber, modelled by  $\widehat{\mathbf{f}}^{\text{ALE}}$ , from the one of the LAA which is separately described by  $\widehat{\mathbf{f}}_{\text{LAA}}^{\text{ALE}}$ .

A correct calibration of this two functions generates a displacement which can be adapted to the LAA morphology. Moreover, by introducing this distinction, we have control on the LAAEF, which can be set to be coherent with the medical statistics concerning the pathologic situation of the patient, providing hence a better estimate of the blood motion inside the most dangerous region in terms of thrombous formation [66, 67, 68].

We define the global component  $\widehat{\mathbf{f}}^{\text{ALE}}$  as:

$$\widehat{\mathbf{f}}^{\text{ALE}}(\widehat{\mathbf{x}}) = \widehat{\psi}(\widehat{\mathbf{x}}) (\widehat{\mathbf{x}} - \widehat{\mathbf{x}}_G), \quad (14)$$

where the second term is a vector field centered in the center of mass of the atrium  $\widehat{\mathbf{x}}_G$ . We compute the function  $\widehat{\psi}$  as a normalized product:

$$\widehat{\psi}(\widehat{\mathbf{x}}) = \frac{\widehat{\varphi}(\widehat{\mathbf{x}}) (1 - \widehat{\varphi}(\widehat{\mathbf{x}}))}{\max_{\widehat{\mathbf{x}} \in \partial\widehat{\Omega}} \{\widehat{\varphi}(\widehat{\mathbf{x}}) (1 - \widehat{\varphi}(\widehat{\mathbf{x}}))\}}, \quad (15)$$

being  $\widehat{\varphi}$  solution of the following Laplace-Beltrami problem [69]:

$$\begin{cases} -\Delta_{\Gamma} \widehat{\varphi} = 0 & \text{in } \partial\widehat{\Omega}, \\ \widehat{\varphi} = 0 & \text{on } \bigcup_{j=1}^4 \widehat{\Gamma}^{\text{PV}_j}, \\ \widehat{\varphi} = 1 & \text{on } \widehat{\Gamma}^{\text{MV}}. \end{cases} \quad (16)$$

By defining  $\widehat{\psi} : \partial\widehat{\Omega} \rightarrow [0, 1]$  as described, we get a smooth function which is zero on the inlet and outlet sections of our computational domain, and non-null in the main chamber, as displayed in Figure 5.

Analogously, we construct the function  $\widehat{\mathbf{f}}_{\text{LAA}}^{\text{ALE}}$  as follows:

$$\widehat{\mathbf{f}}_{\text{LAA}}^{\text{ALE}}(\widehat{\mathbf{x}}) = \widehat{\Psi}(\widehat{\mathbf{x}}) \widehat{\xi}(\widehat{\mathbf{x}}) (\widehat{\mathbf{x}} - \widehat{\mathbf{x}}_G^{\text{LAA}}), \quad (17)$$

where  $\widehat{\mathbf{x}}_G^{\text{LAA}}$  is the center of mass of the LAA and in this work we define for simplicity  $\widehat{\Psi}$  as:

$$\widehat{\Psi}(\widehat{\mathbf{x}}) = k \widehat{\psi}(\widehat{\mathbf{x}}). \quad (18)$$

The use of a multiplicative constant  $k$  in Equation 18 allows us to vary the importance of the LAA contraction, according to the LAAEF, which characterizes the pathological situation of the patient. By defining  $\widehat{\mathbf{f}}_{\text{LAA}}^{\text{ALE}}$  as explained, we get a displacement which is directed towards the center of mass of the LAA; moreover, it is fundamental the use of a function  $\widehat{\xi}$  to localize the support only at the LAA surface, indeed the changes need to be located only in this region<sup>1</sup>.

#### 4. Setup of numerical simulations

We carried out numerical simulations four ideal patients. In particular, we consider a LA geometry related to a patient in physiologic conditions, assuming first sinus rhythm and then AF, and two geometries of patients really affected by AF. The geometries are patient-specific and obtained from medical images available from [36], and openly accessible in the supplementary material of [34, 35]. The imaging method used to reconstruct the medical images is a Diffusion Tensor Magnetic Resonance Imaging (DTMRI), which allows a better resolution of the thin atrial wall [36]. The hearts were of donors from National Disease Research Interchange (Philadelphia, PA).

<sup>1</sup>We remark that by using an identity function to localize the support may cause discontinuities which can lead to a “break” of the surface, for this reason we apply a mollifier to avoid this problem.

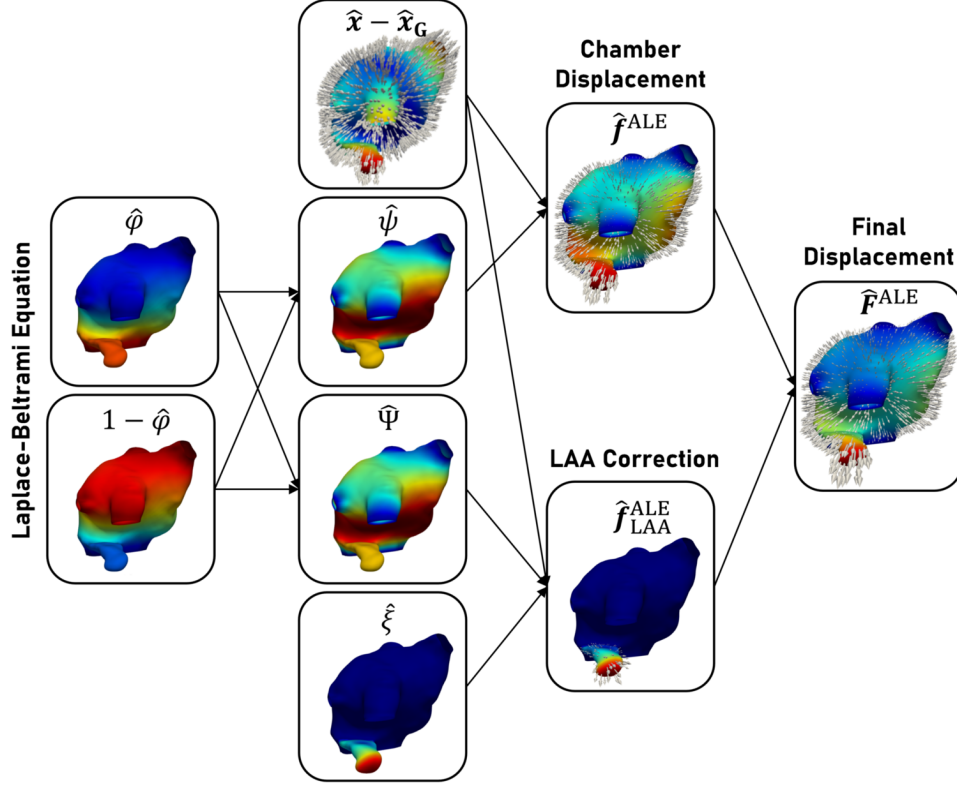


Figure 5: Complete procedure to derive the displacement function  $F^{\text{ALE}}$  starting from the Laplace-Beltrami solutions (concerning  $\hat{\varphi}$ ,  $1 - \hat{\varphi}$ ,  $\hat{\psi}$  and  $\hat{\xi}$  red and blue correspond to 1 and 0, respectively).

The geometrical and clinical information of the three patients are resumed in Table 1.

In Table 2, we list the Left Atrial Ejection Fraction (LAEF) and LAAEF computed after our procedure, and defined as:

$$\text{LAEF} = \frac{V_{\text{LA}}^{\text{max}} - V_{\text{LA}}^{\text{min}}}{V_{\text{LA}}^{\text{max}}}, \quad \text{and} \quad \text{LAAEF} = \frac{V_{\text{LAA}}^{\text{max}} - V_{\text{LAA}}^{\text{min}}}{V_{\text{LAA}}^{\text{max}}}, \quad (19)$$

respectively. We remark that the maximum volumes are directly retrieved by medical images; whereas the minimum ones are determined after the application of the displacement.

The volumes of patients AF2 and AF3 are larger than the ones normally detected in physiologic conditions. These values suggest an atrial remodeling caused by the AF pathology; hinting at the possibility of a persistent AF. As reported in Table 2, the in-silico values we compute are in accordance with the clinical measurements, for both LAEF [70, 72, 71], and LAAEF [49], making the whole displacement procedure significant and reliable.

<b>Geometry</b>	<b>P1</b>	<b>P2</b>	<b>P3</b>
<b>Age</b>	55 Years	86 Years	94 Years
<b>Gender</b>	Male	Male	Female
<b>Pathology</b>	None	AF	AF
<b>LA Max Volume [cm<sup>3</sup>]</b>	58.06	85.55	69.39
<b>RA Max Volume [cm<sup>3</sup>]</b>	69.39	55.76	36.33

Table 1: Information of the geometries detected from images

<b>Patient (Geometry)</b>	<b>Pathology</b>	<b>Indicator</b>	<b>Value</b>	<b>Clinical measurement</b>	<b>Reference</b>
<b>PH1 (P1)</b>	None	LAEF (%)	50.49	45.1 ÷ 64.1	[70]
		LAAEF (%)	77.81	62.5 ÷ 86.5	[49]
<b>AF1 (P1)</b>	Paroxysmal AF	LAEF (%)	30.72	10.0 ÷ 50.0	[71]
		LAAEF (%)	62.72	50.0 ÷ 69.0	[49]
<b>AF2 (P2)</b>	Persistent AF	LAEF (%)	18.48	6.0 ÷ 26.0	[71]
		LAAEF (%)	38.94	32.4 ÷ 63.2	[49]
<b>AF3 (P3)</b>	Persistent AF	LAEF (%)	21.17	6.0 ÷ 26.0	[71]
		LAAEF (%)	53.45	32.4 ÷ 63.2	[49]

Table 2: Patients information from images and modeling assumptions, the clinical measurement are intended in a range (min÷max)

#### 4.1. Results of lumped-parameter model

The parameter values used in the simulation of the lumped-parameter model have to be calibrated, starting from values present in the literature [73, 38, 74, 75, 39]. However, due to the requirement to fit the information from medical images and pathological situation, they need to be adjusted separately for each single patient. We report the parameters that we keep common to all cases in Table A.8. Instead, in Table A.9, we store the chambers elastances differentiating the 4 simulated cases.

We report the LA volume, pulmonary venous flowrate and pressure and ventricular pressure in Figure 6, for the four cases simulated. We recall that these functions are taken as output from the 0D model and employed as boundary data for our 3D CFD simulation. As we can see, we have two primary changes in pressures distribution. We detect a smaller maximum value of the left ventricular pressure, which is a realistic pathological consequence of AF [64, 63]. The second change is an increase of the pulmonary venous pressure, which is also a common effect of the pathology [61]. In the AF case, we have less variation of the pulmonary venous flow rate, in particular we have smaller values due to the reduced LAEF. Indeed, AF cases do not show the ‘‘atrial kick’’ due to the reduced contractility deriving from the incorrect action potential diffusion [2, 4].

#### 4.2. Meshes

As we can see in Figure 7, we build a hexahedral mesh with an heterogeneous size  $h_K$ . Indeed, we perform a refinement in the LAA to catch the geometrical features of this region, and near the MV, to correctly represent the valve via the RIIS method. Indeed, we use a value of  $\varepsilon = 1.3$  mm due to the medical estimates of 2.6 mm of MV leaflet thickness [76, 77] ( $\varepsilon$  represents

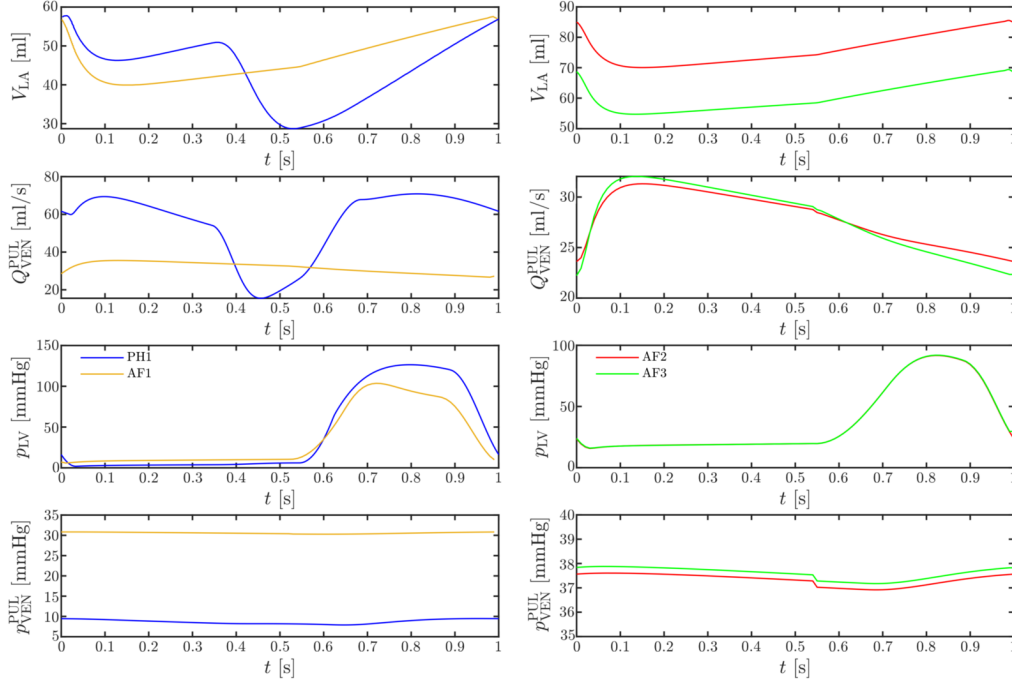


Figure 6: Results of the lumped-parameter model simulations, used then to impose the boundary conditions.

the half-thickness of the valve leaflets). Concerning opening  $\Delta\tau_O$  and closure  $\Delta\tau_C$  duration of the MV, we consider literature estimates, and we set  $\Delta\tau_O = 20$  ms [78] and  $\Delta\tau_C = 60$  ms [79]. We consider the opening of the valve when the pressure of a control volume inside the LA is higher than the one computed inside a volume downwind the valve. The valve closure starts at a fixed time, imposed when  $\dot{V}_{LV}$  of the 0D model simulation becomes negative, i.e. when a condition of reversed flow is detected on the outlet section [80].

The MV geometries were not available in the repository [34, 35]. For this reason, we adapt the MV geometries provided by Zygotte [81] to the mitral orifice of the patient-specific LA. The procedure to adapt the Zygotte valve to the patient-specific geometry is given in [82]. Moreover, the leaflet displacement is the same used in [41].

By using the VMTK library [83], we first generate a tetrahedral mesh, then we use mesh tetex [84] to obtain an hexaedral mesh in which each tetrahedron is split into four hexaedra preserving the aspect ratio of the original element. The information about the constructed meshes are reported in Table 3.

## 5. Numerical simulations

The computational solver is based on a GMRES method for the resolution of the linear system at each time step. The linear system is preconditioned with the aSIMPLE preconditioner [85] and its blocks are preconditioned with an algebraic multigrid preconditioner based on Trilinos [86].

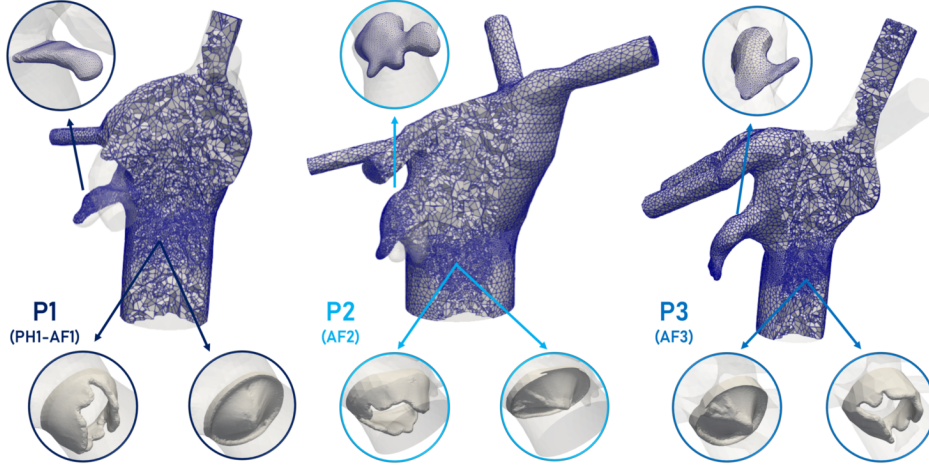


Figure 7: Meshes used to simulate the patients haemodynamics, with the detail of: LAA morphology, the MV in open and closed configurations as described by the RIIS method.

<b>Mesh (Patient)</b>	<b>P1 (PH1-AF1)</b>	<b>P2 (AF2)</b>	<b>P3 (AF3)</b>
<b>Number of Cells</b>	120 860	182 540	110 472
<b>Velocity DOFs</b>	411 873	614 631	378 879
<b>Pressure DOFs</b>	137 291	204 877	126 293
<b>Total DOFs</b>	549 164	819 508	505 172
$h_K^{\max}$ [mm]	5.95	5.44	6.15
$h_K^{\min}$ [mm]	0.43	0.40	0.38
$h_K^{\text{avg}}$ [mm]	1.76	1.69	1.82

Table 3: Properties of the meshes

All the simulations, based on the mathematical models we have shown, have been executed using `lifex` [87], a high-performance C++ FE library developed within the iHEART project<sup>2</sup>, mainly focused on cardiac simulations and based on `deal.II` finite element core [88]. Numerical simulations are run in a parallel framework<sup>3</sup>

### 5.1. Eulerian indicators

Blood density and dynamic viscosity are set equal to  $\rho = 1.06 \cdot 10^3 \text{ kg/m}^3$  and  $\mu = 3.5 \cdot 10^{-3} \text{ kg/(m} \cdot \text{s)}$ , respectively. We simulate six heartbeats of period  $T_{\text{HB}} = 1 \text{ s}$ , starting from

<sup>2</sup>iHEART - An Integrated Heart model for the simulation of the cardiac function, European Research Council (ERC) grant agreement No 740132, P.I. Prof. A. Quarteroni, 2017-2022

<sup>3</sup>Numerical simulations are carried out on the cluster of the Department of Mathematics, Politecnico di Milano. Specifically, simulations PH1, AF1 and AF2 were executed on the queue Gigat (6 nodes, 12 Intel Xeon E5-2640v4 @ 2.40GHz, 120 cores, 384GB RAM, O.S. Centos 6.7) using 2 nodes with 20 cores each, and AF3 was executed on cluster Gigatlong (5 nodes, 10 Intel Xeon Gold 6238 @ 2.10GHz, 280 cores, 2.5TB RAM) using 1 node with 56 cores.

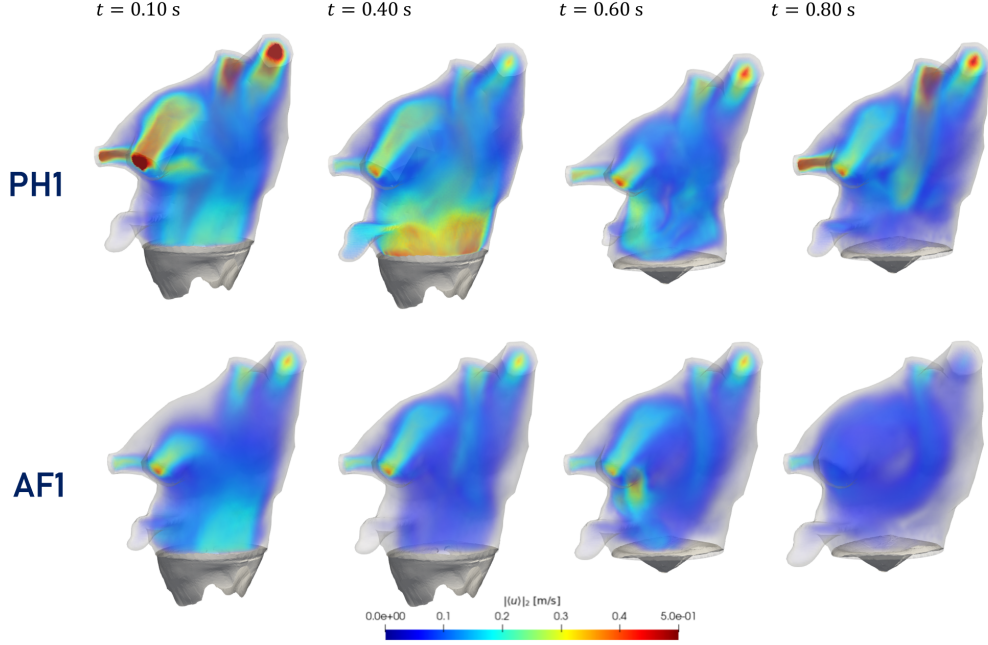


Figure 8: Volume rendering of phase-averaged velocity magnitude  $|\langle \mathbf{u} \rangle|_2$  at different time instants in physiologic and AF conditions.

a null initial condition. However, to filter out the unphysical consequences of this choice, we discard the first two heartbeats and we consider the phase-averaged velocity, defined over  $N_{\text{HB}}$  heartbeats, as:

$$\langle \mathbf{u}(\mathbf{x}, t) \rangle = \frac{1}{N_{\text{HB}}} \sum_{n=1}^{N_{\text{HB}}} \mathbf{u}(\mathbf{x}, t + (n-1)T_{\text{HB}}), \quad (20)$$

where  $N_{\text{HB}} = 4$  in our case.

In Figure 8 we report the velocity magnitude in Figure 8 during a heartbeat. The velocity magnitude is larger in physiologic conditions than in AF ones during the whole heartbeat. This behaviour is evident during the E-wave ( $t \approx 0.10$  s), whereas the A-wave is present only in the patient PH1, at time 0.40 s. When the MV is closed, we can notice the difference in the contraction of the two atrial chambers, due to the contractile reduction in fibrillation ( $t \approx 0.60$  s).

In Table 4, we report velocity statistics about patients PH1 and AF1. We validate the peak velocities during the heartbeat at the pulmonary veins inlet in comparison with estimates from MRI images [89]. Moreover, we perform a validation comparing the peak and mean velocities inside the whole LA with medical estimates from MRI images in [89, 8]. All the values we compute starting from our simulations are consistent with the ranges present in the medical literature. The lack of information about the peak velocities in persistent AF does not allow to validate the remaining two simulations in terms of these indicators.

In Figure 9, we can qualitatively observe the absence of A-wave also in cases AF2 and AF3, which show lower magnitude values of the velocity field in all the cardiac chamber. The inlet

Patient	Indicator	<i>In silico</i> result	Clinical measurement	Reference
PH1	Peak velocity veins [m/s]	0.474	0.370 ÷ 0.600	[89]
	Peak velocity [m/s]	0.775	0.560 ÷ 1.060	[89]
	Mean velocity [m/s]	0.149	0.130 ÷ 0.170	[8]
AF1	Peak velocity veins [m/s]	0.276	0.250 ÷ 0.540	[89]
	Peak velocity [m/s]	0.480	0.470 ÷ 0.970	[89]
	Mean velocity [m/s]	0.096	0.080 ÷ 0.140	[8]

Table 4: Velocity statistics in LA and at pulmonary veins entrance for cases PH1 and AF1 in comparison

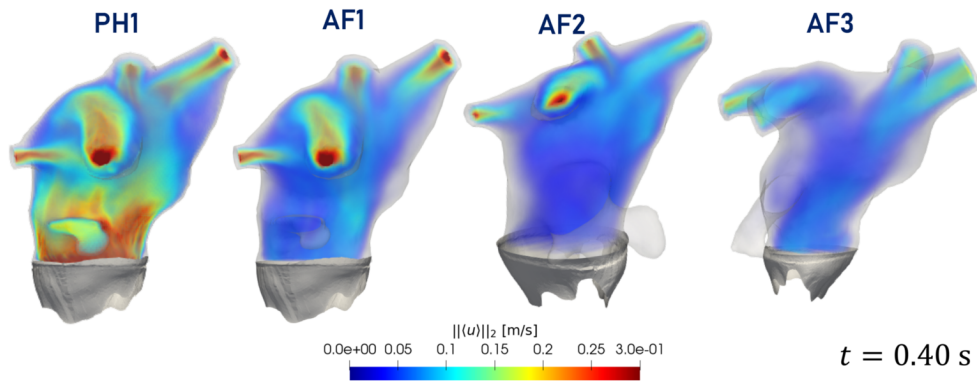


Figure 9: Volume rendering of phase-averaged velocity magnitude  $\|\mathbf{u}\|_2$  during the A-wave in all the patients.

velocity at the pulmonary vein is significantly lower in patient AF3. This might be related to the geometrical differences between patients; as a matter of fact, AF3 is characterized by a small atrial chamber and large veins. Finally, we notice that velocities in LAA are particularly low. This is due to the higher risk of thrombotic formation in this region [66, 67, 68].

We report the velocities computed at the MV section in Figure 10 and we compare our results with the literature estimates from Doppler imaging [90, 91, 92]. The value is computed by space-averaging the velocity values inside a spherical volume between the leaflet of MV, coherently with the procedure used starting from Doppler images. The peak velocity detected both in physiologic and AF conditions are coherent with the medical estimates, as we show in Table 5. The case PH1 allows also to perform a validation with the A-wave, not present in AF, peak velocity and then with the E/A ratio, which is an important medical parameter [92, 91]. All the values found are coherent with the ones present in the medical literature.

#### Flow stasis indicator

The flow stasis is an indicator representing the fraction of time of the heartbeat in which the velocity magnitude in a specific point is smaller than 0.1 m/s [93]. Starting from this indication, we define it as follows:

$$F_S(\hat{\mathbf{x}}) = \frac{1}{T_{\text{HB}}} \int_0^{T_{\text{HB}}} \chi_{\{\|\mathbf{u}\|_2 < 0.1 \text{ m/s}\}}(\hat{\mathbf{x}}, t) dt \quad \text{in } \widehat{\Omega}, \quad (21)$$



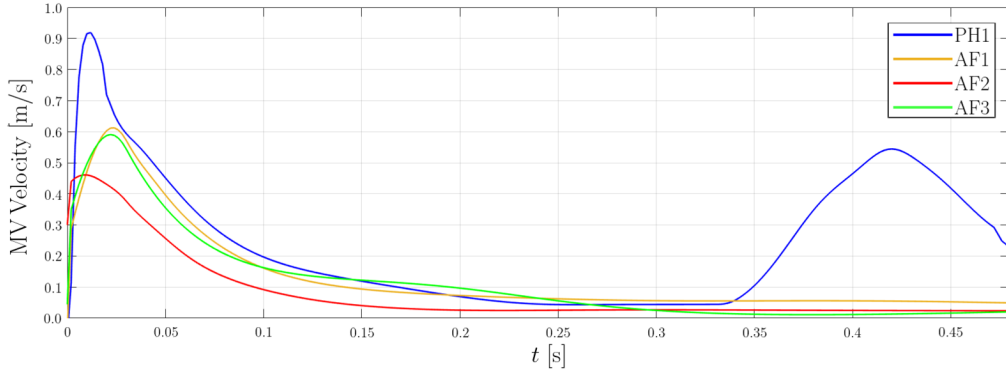


Figure 10: MV transmitral velocity profiles in the four patients.

Patient	Indicator	<i>In silico</i> result	Clinical measurement	Reference
PH1	E-peak velocity [m/s]	0.918	0.740 ÷ 1.040	[91]
	A-peak velocity [m/s]	0.544	0.520 ÷ 1.040	[91]
	E/A ratio [-]	1.68	0.800 ÷ 1.870	[92, 91]
AF1	E-peak velocity [m/s]	0.612	0.443 ÷ 0.771	[90]
AF2	E-peak velocity [m/s]	0.664	0.516 ÷ 0.812	[90]
AF3	E-peak velocity [m/s]	0.591	0.516 ÷ 0.812	[90]

Table 5: Transmitral velocities parameters: peak velocities in early wave (for all cases) and after wave (in physiologic conditions), together with the E/A ratio for PH1.

where  $\chi$  is a characteristic function. An accurate estimate of the flow stasis is fundamental to determine a thromboembolic risk, which is typically related to AF pathologies [5]. Indeed, two centuries ago, it was defined the “Virchow’s triad” to denote the three main factors contributing to thrombosis risk: endothelial injuries, hypercoagulability and blood stasis [94].

The computed flow stasis fields can be observed in Figure 11. We notice larger stasis values in AF conditions, which is coherent with the slower velocities we found, and it is also confirmed by the medical estimates, provided by the 4D flow MRI data available in the literature [8, 93, 95]. However, due to the lower quality of the imaging compared with the CFD resolution and to the patient dependence of the haemodynamics, making an exact comparison with the magnitude of the medical estimated maps is difficult. For this reason, we compute some mean values as reported in Table 6. The average procedure is first performed by considering the whole chamber, and then it is repeated neglecting a 3 mm of the boundary layer, coherently with the medical literature [9]. Indeed, in this way, we obtain values within the reference ranges; on the contrary, considering the total value, the effect of the boundary layer presence in simulations is to overestimate the stasis. For this reason, we will also propose a new indicator in Section 5.3, which overcomes this inconvenient and couples the stasis information with the blood age.

#### *Time-averaged wall shear stress*

The shear stress at the wall is related to endothelial shear, formation of new tissues and plaques, and promoting of neointimal hyperplasia [96]. We can define the wall shear stress

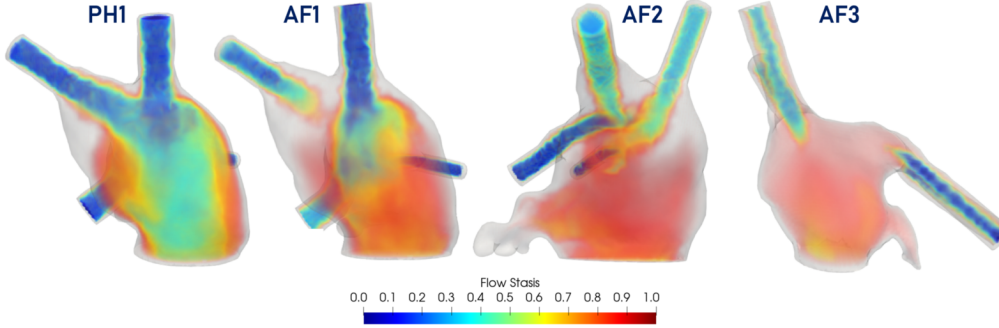


Figure 11: Volume rendering of the flow stasis indicator in all the four cases.

Patient	<i>In silico</i> result	Clinical measurement	Reference
PH1	0.333	0.128 ÷ 0.502	[9, 93]
AF1	0.806	0.222 ÷ 0.896	[9, 93]
AF2	0.853	0.222 ÷ 0.896	[9, 93]
AF3	0.873	0.222 ÷ 0.896	[9, 93]

Table 6: Flow stasis average values of the four cases.

(WSS) vector on the boundary  $\partial\widehat{\Omega}$  as follows:

$$\tau_w(\langle \mathbf{u} \rangle) = \tau(\langle \mathbf{u} \rangle) \cdot \mathbf{n} - (\tau(\langle \mathbf{u} \rangle) \cdot \mathbf{n})\mathbf{n} \quad \text{on } \partial\widehat{\Omega}, \quad (22)$$

where  $\tau(\langle \mathbf{u} \rangle) = 2\mu\mathbf{D}(\langle \mathbf{u} \rangle)$  is the viscous stress tensor and  $\mathbf{D}(\langle \mathbf{u} \rangle) = \frac{1}{2}(\nabla\langle \mathbf{u} \rangle + \nabla^\top\langle \mathbf{u} \rangle)$ . We compute the parameter on the reference configuration  $\partial\widehat{\Omega}$  provided by the medical images, with the perspective of computing a time-averaged indicator.

Specifically, we consider the time-averaged wall shear stress (TAWSS) defined as [22]:

$$\text{TAWSS}(\langle \mathbf{u} \rangle) = \frac{1}{T_{\text{HB}}} \int_0^{T_{\text{HB}}} |\tau_w(\langle \mathbf{u} \rangle)|_2 dt, \quad \text{on } \partial\widehat{\Omega} \quad (23)$$

In Figure 12, we report the TAWSS for all the patients. The results confirm that in AF cases, we obtain smaller values than in physiologic conditions. This is significant, in particular considering the same geometry by comparing PH1 and AF1. This is associated to a sensibly higher thrombosis risk in patients affected by AF. In general, we reach the minimum values on the final part of LAA surface, coherently with the medical literature [66, 67, 68]. However, in AF2 the morphology of the atrium allows larger values in the first part of the appendage, which is large and allows the formation of some vortices, causing a better washout of the LAA. On the contrary, the morphology of the appendage of patient AF3, causes a slower blood flux, due to its flat morphology.

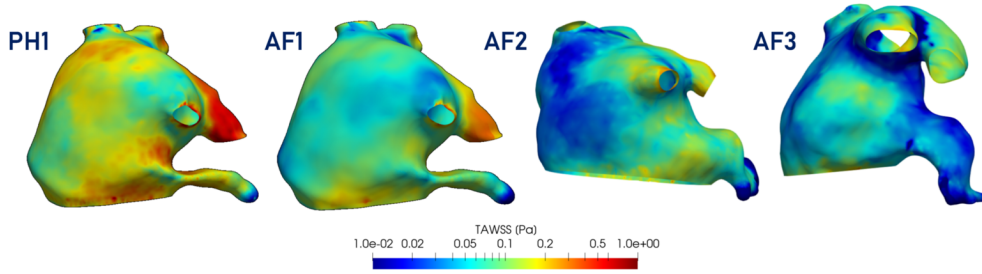


Figure 12: TAWSS indicator in all the patients.

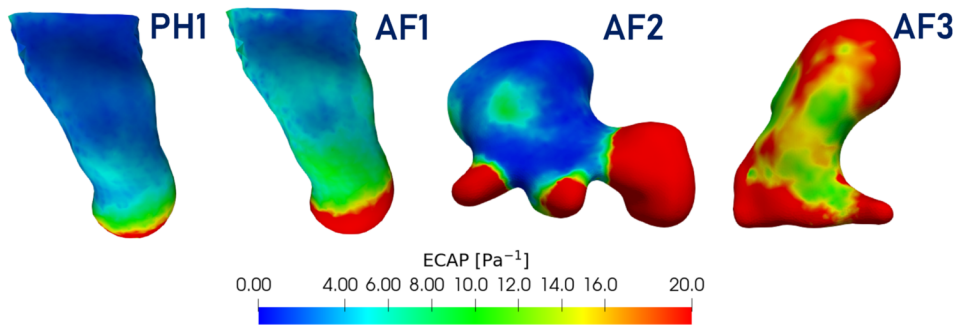


Figure 13: ECAP indicator in all the LAAs.

#### *Endothelial Cell Activation Potential*

Another commonly used indicator to detect the endothelial susceptibility and the thrombus formation probability is the Endothelial Cell Activation Potential (ECAP) indicator [97], defined as:

$$ECAP(\langle \hat{\mathbf{u}} \rangle) = \frac{OSI(\langle \hat{\mathbf{u}} \rangle)}{TAWSS(\langle \hat{\mathbf{u}} \rangle)}, \quad (24)$$

being OSI the Oscillatory Shear Index [96]. OSI is high in regions where the WSS changes much during the heart cycle. Thus, ECAP detects high oscillatory and small shear stresses regions.

In Figure 13, we focus on the LAA wall where we measure large values of ECAP, confirming the location of high thrombosis risk [66, 67, 68]. Concerning patient AF2, we observe a risk of thrombosis principally located in the apical part of LAA, after the separation in three components. Patient AF3 shows high values of ECAP along the whole appendage, due to the conformation and to the advanced simulated pathology. These results are coherent with the ones obtained from other patient-specific studies present in literature [98, 32], correlating the LAA geometries to the ECAP spatial distribution.

The Eulerian analysis clearly shows the higher risk of thrombosis formation in AF and located in LAA, considering different types of indicators, connected both to two parameters of the Virchow's triad: blood stasis (flow stasis and  $|\langle \mathbf{u} \rangle|_2$ ) and endothelial susceptibility (TAWSS and ECAP). However, the limit of the Eulerian analysis is the absence of historical notions about the blood flow, connected with the particles path, and only detectable using a Lagrangian perspective.

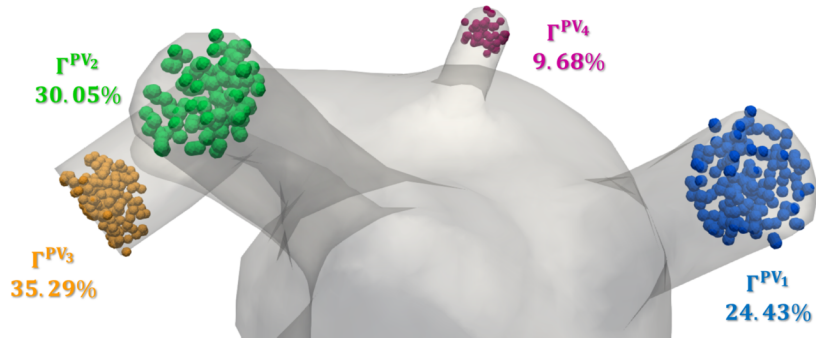


Figure 14: Position of parcels injection in cases PH1 and AF1.

## 5.2. Lagrangian indicators

The detection of indicators from the realization of a Lagrangian simulation can be useful to detect additional information about the haemodynamic differences between physiologic and pathologic patients [16]. We carry out numerical simulations of the red blood cells movement inside the LA, using as velocity field the result of our NS simulations presented in Section 4. In addition, we consider the introduction of  $N_H$  parcels<sup>4</sup> at any heartbeat. In particular, we consider the injection of a volume of blood  $V_{inj}$  computed as:

$$V_{inj} = \int_0^{T_{HB}} Q_{VEN}^{PUL}(t) dt. \quad (25)$$

We use the injected volume to estimate the number  $N_P$  of entering cells in the atrium during a single heartbeat, considering also that the number of red blood cells in a cubic millimetre is around 5 millions [100]. Our simulation is designed to get a constant approximated weight  $\omega = N_P/N_H \simeq 1409$ , common to all cases, where  $N_P$  is the number of simulated red blood cells.

The number of parcels injected at any timestep can be computed as follows:

$$n_H(t) = \frac{Q_{VEN}^{PUL}(t)}{V_{inj}} \Delta\tau N_H, \quad (26)$$

where  $\Delta\tau$  is the time step we choose for the Lagrangian simulation. We split the injection among the four pulmonary veins according to the flow repartition factor introduced in Equation 4; the parcels are distributed in a hemisphere centered at the beginning of the pulmonary vein extension and with the same radius of the cylinder. The initial position of the parcels is randomly chosen inside the hemisphere and an example can be observed in Figure 14.

More information about the equation of motion of the parcels and the construction of Eulerian fields from the Lagrangian perspective can be found in Appendix B.

<sup>4</sup>A parcel  $j$  is a macro-particle associated to a number  $\omega_j$  of real particles, in our case red blood cells. This numerical approximation is typical of the Discrete Parcel Method (DPM) [99]. The complete definition of the concept can be found in Appendix B

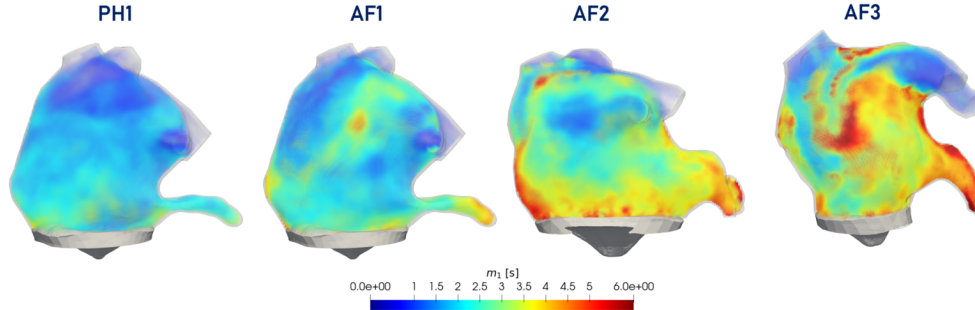


Figure 15: Blood mean age field  $m_1$  in seconds in the four patients volume rendering.

### *Mean age of blood*

We consider the injection of particles during all the simulated cardiac cycles to construct some Eulerian fields from the Lagrangian perspective, with the information of all the simulated heartbeats. The computation of results based on the age of the blood gives us a new perspective to analyse the regions in which the particles remain for a long time in the atrium, increasing the thrombosis. Additional details on the definition of this field can be found in Appendix B.

The mean age field of red blood cells detects regions in which the blood particles stagnate in the atrium. This indicator was proposed by [18] to analyse the age of the blood in the LA subjected to AF. We denote it as  $m_1$  and its definition is provided in Appendix B.

In Figure 15, we can observe the  $m_1$  field for the four simulated cases. We observe that regions with the largest values are near the boundary of the MV orifice and in the LAA. In AF conditions, the regions where the mean age field is greater or equal to 3 s are much more than in the physiologic case. The differences are evident in particular considering the persistent fibrillation of patients AF2 and AF3, probably due to higher volumes, lower velocities and smaller ejection fractions.

### *Washout of blood*

We compute the washout field  $\psi_{\bar{t}}$  at the final time, as defined in Appendix B. In particular, in the simulation we choose  $\bar{t} = 2$  s, we consider a contribution to the field equal to 1 from the particles injected in the first two cycles and equal to 0 for the others. The resulting field gives values between 0 and 1, where:

- $\psi_{\bar{t}} \gtrsim 0$ , means we have local prevalence of particles injected after  $\bar{t}$ ;
- $\psi_{\bar{t}} \lesssim 1$ , means we have local prevalence of particles injected before  $\bar{t}$ .

Intermediate values are achieved in regions in which we do not have a prominent prevalence.

In Figure 16, we can observe the field at time  $t = 6$  s in the LA volume. The field becomes transparent as approaches 0, in order to highlight the regions with slow blood flow. In this case, the washout assumes quite small values in the whole domain. In patients affected by AF, the washout field shows an incomplete turnover of the blood in the lower part of the atrial chamber, in particular considering the LAA. However, distinct geometries show some differences: in patient AF3, we find a better washout in the atrial chamber than patient AF2, represented by the more

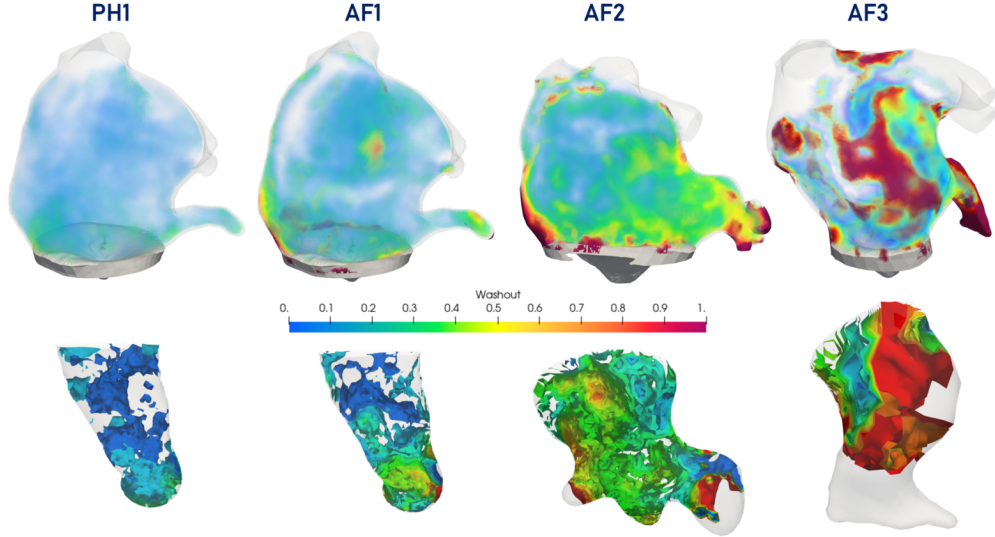


Figure 16: Washout field  $\psi_2$  in the four patients LA (volume rendering in upper row) and LAA (isosurfaces  $\psi_{\bar{t}} = k/10$  for  $k = 1, 2, \dots, 10$  in lower row) at time  $t = 6$  s.

diffuse transparency inside the domain In Figure 16. At the same time, patient AF3 has more static blood inside the appendage, despite a higher ejection fraction, and near the boundaries.

We display the isosurfaces  $\psi_{\bar{t}} = k/10$  for  $k = 1, 2, \dots, 10$  in the LAA in Figure 16. These surfaces clearly show differences between PH1 and AF1. Concerning the initial part of the LAA, we cannot detect differences in the washout values in the two cases. On the contrary, at the apical part of the appendage, we have less exchange of blood, coherently with the lower LAEEF imposed.

#### *Residence time and total path length*

In this section, we consider the injection of particles during the first heartbeat only, and we analyze the distributions of some Lagrangian indicators in the following 5 heartbeats of simulation we have at our disposal. In particular, we consider the distribution of the Total Path Length (TPL), being the length travelled by a parcel before leaving the LA, and the Residence Time (RT) which is the time spent by a parcel inside the LA. We report the indicators distributions and a scatter plot correlating RT and TPL in Figure 17. First, we can notice that the particles in AF conditions follow shorter paths coherently with the lower velocities we detected in the blood (as shown Figure 9). Moreover, in case PH1, we have a larger amount of particles which leaves the LA faster, a result consistent with the larger LAEEF found in Table 2.

Finally, we observe that not all the parcels remaining for a long time in the chamber cover comparable paths. As a matter of fact, considering the same residence time, some parcels travel long paths, whereas others cover smaller paths, making hence the blood more stagnant. The last ones can cause blood clots formation in LA. The difference between these two types of paths suggest that the analysis of the mean age field cannot provide a complete analysis of thrombosis risk; to complement the indicator we couple it with the flow stasis to obtain a more comprehensive indicator in Section 5.3.

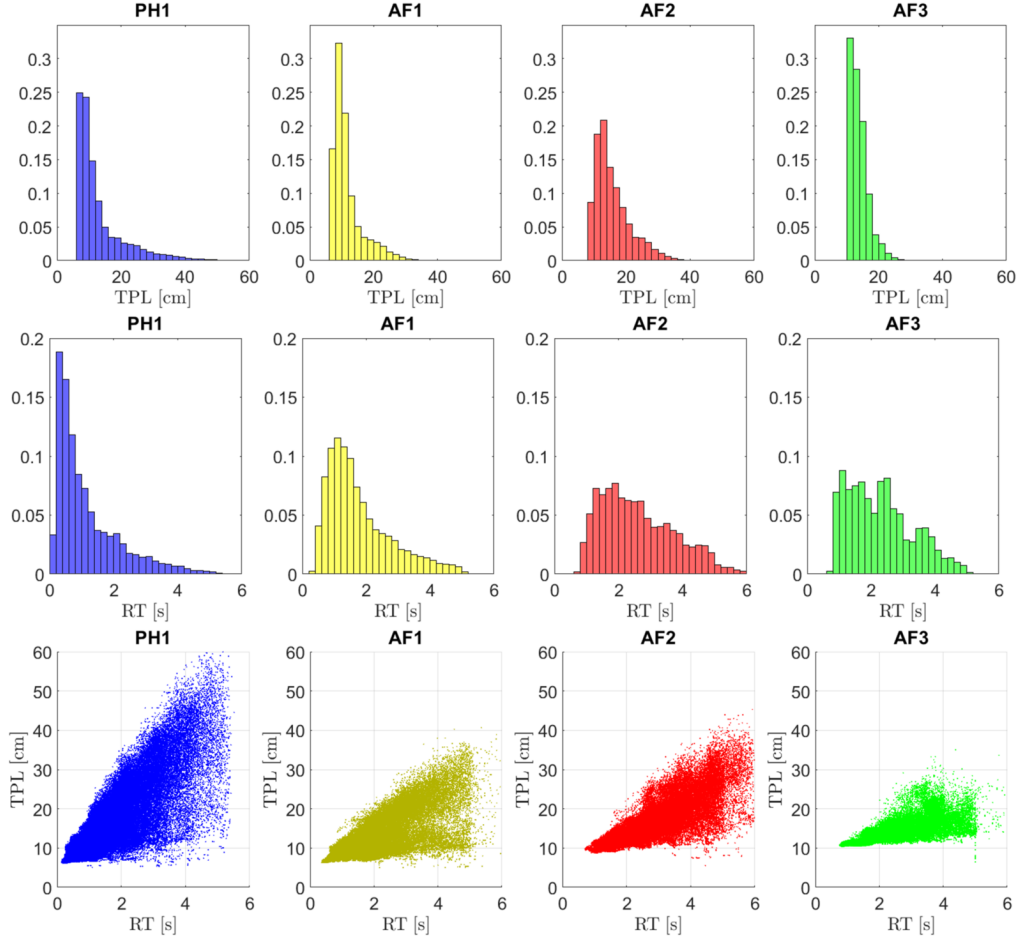


Figure 17: TPL histogram distribution (first row), RT histogram distribution (second row) and correlation scatter plot (third row)

### 5.3. Age Stasis: a new haemodynamic indicator

In order to summarise the high complexity of the blood flow inside the LA, we introduce a novel haemodynamic indicator, that we call Age Stasis (AS), by combining results from both the Eulerian and Lagrangian analyses of the haemodynamics in LA. Our goal is to construct an indicator which considers, at the same time, information about the stagnation of the flow and the oldness of the blood cells, which are two main aspects in thrombus formation. We define AS as:

$$A_S(\mathbf{x}) = F_S(\mathbf{x}) \frac{m_1(\mathbf{x})}{T}, \quad (27)$$

in this way, we are constructing an indicator which accounts for the flow stasis  $F_S(\mathbf{x})$ , that localizes regions in which the blood flows slowly, and a relative mean age of the blood  $m_1(\mathbf{x})$ . Thus, we can distinguish regions in which the flow is slow and the particles present are old ( $A_S \simeq 1$ ). In the detection of dangerous regions, we neglect ( $A_S \simeq 0$ ) the ones in which:

Parameter	PH1	AF1	AF2	AF3
$V_{AS(0.1)}/V_{LA}$	41.3%	11.7%	5.70%	4.20%
$(V_{LA} - V_{AS(0.5)})/V_{LA}$	0.70%	5.50%	23.3%	27.5%

Table 7: Age Stasis Volumes (%) significant values

- the flow is slow ( $F_S \simeq 1$ ) but the particles are not old ( $m_1 \ll T$ ); so there are no particles stationing at that point for a long time. In particular, the boundary layers, where the flow stasis is high, are not always associated with a high thrombosis risk;
- the flow is fast ( $F_S \simeq 0$ ) but the particles are old ( $m_1 \simeq T$ ). These regions are the ones that require more time to be reached by particles because of their location, but which are not stationing points. These regions are not at risk of thrombi formation, because of the absence of the stasis factor. The mitral orifice is the best example of this scenario.

The result is a useful dimensionless indicator which assumes values between 0 and 1. We use this indicator to investigate the percentage of the volume which is associated to the thrombogenic risk, by introducing the Age Stasis Volume function, that we define as:

$$V_{AS}(\theta) = \int_{\Omega} \chi_{\{A_S(x) \leq \theta\}} \mathbf{d}\mathbf{x}, \quad (28)$$

This function, given a value  $\theta$  of  $A_S$ , returns the volume  $V_{AS}(\theta)$  of blood inside the LA characterized by a value of AS smaller than  $\theta$ .

A comparison between the Age Stasis Volume functions computed in the four simulated cases is provided in Figure 18. The cumulative distributions show that the percentage of volume associated to low values of stasis is significantly higher in physiological than in AF conditions, for each value of AS. We can observe the same trend by making a comparison between paroxysmal and permanent AF cases. For this reason, we can infer a relation among the resulting curve and the severity of the pathology.

By choosing a specific value of  $A_S = 0.1$ , we obtain the results in Table 7. The results show that, in PH1, more than the 40% of the total volume is associated to values of AS smaller than this threshold. On the contrary, in the AF situations we have a sensible reduction of the volume. Moreover, for AF2 and AF3, there are smaller values (5 – 6%) than in AF1 case ( $\simeq 10\%$ ), coherently with the persistence of AF in those cases.

Another interesting result is the evaluation of the volume percentage which presents a value of AS larger than 0.5. In this way, we are quantifying the regions in which we have higher thrombogenic risk. The results in Table 7 confirm that there is a higher risk in fibrillation cases. In particular, in advanced pathologies, the percentage of volume associated to this risk is around a quarter of the total; on the contrary, in physiologic conditions, we detect a percentage smaller than 1%.

Finally, in Figure 19, we display the distribution of the AS values in the LA volume, constructed using a random sampling of the domain. The PH1 case distribution is different from the others due to the predominancy of low stasis values. AF2 and AF3 show distribution tails that are more consistent in the region of high values of stasis than AF1.



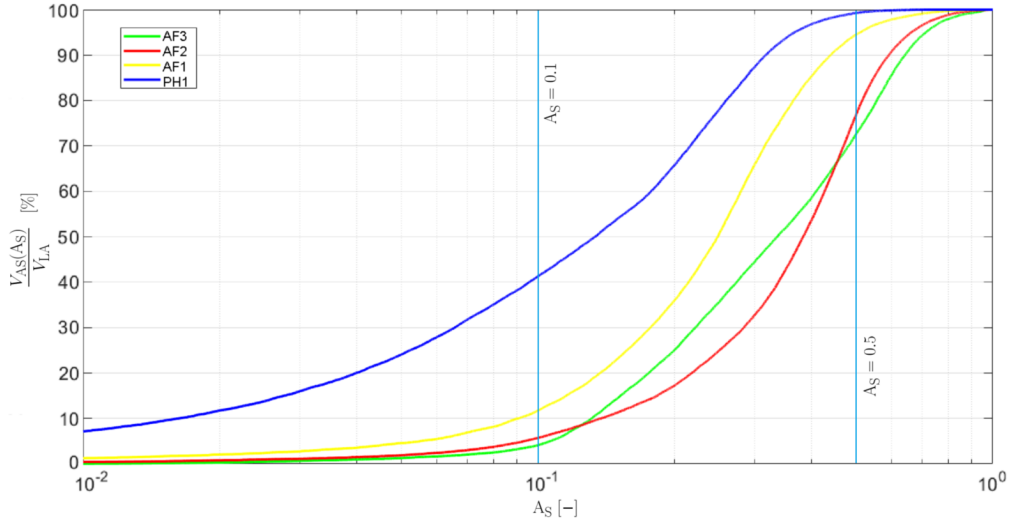


Figure 18: Age Stasis Volume function: comparison between all the simulated cases.

## 6. Conclusions

In this paper, we numerically simulated the left atrial haemodynamics in both physiologic and atrial fibrillation conditions by considering patient-specific geometries and idealized parametrized displacement fields. The numerical results were analyzed from an Eulerian and Lagrangian view point, computing several indicators and biomarkers typically used in literature. Finally, we propose a novel haemodynamic indicator to analyse the risk of thrombosis by combining the two approaches, moreover we use it to compute a synthetic distribution function, which allows performing a quick comparison between different individuals.

We introduced an original procedure aimed at computing pressure, flowrates and a parametric displacement field that serve as boundary conditions for our CFD problem. Specifically, we employ a lumped-parameter 0D circulation model, we tune it to simulate the hemodynamics in either physiological and pathological conditions, being respectful of the geometrical constraints given by the patient-specific atria. We use a “one-way” 0D-3D coupling scheme between the circulation and the 3D CFD problem. We introduce a new parametric displacement field that correctly catches the typical ejection fraction values of the left atria and of their auricles. The proposed procedure allowed to successfully set up the numerical simulation, by obtaining results that are coherent with the medical literature, both in physiologic and pathological conditions.

The Eulerian analysis detected a substantial reduction of blood velocity and shear stresses on the endocardial walls in pathological conditions. The Lagrangian simulations confirmed that AF increases the average time that a single particle spends in the left atrium, and reduces the washout of the chamber. In addition, we found that the intervariability among patients in terms of morphological features of the left atrial appendage has a dramatic impact on its haemodynamics. A large conformation of the appendage entrance can reduce the endothelial susceptibility, improving the washout of the region. Moreover, the possible existence of lobes in the apical part can significantly affect blood dynamics.

Moreover, by coupling the Eulerian and the Lagrangian results, we proposed a novel haemo-

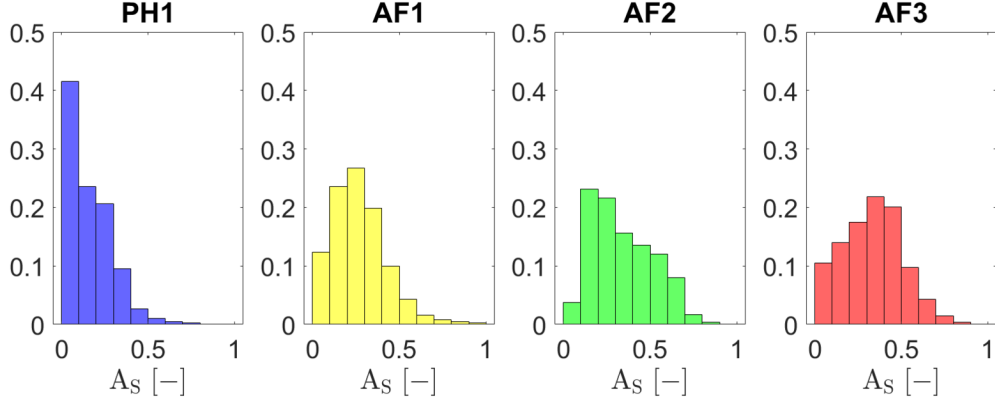


Figure 19: Age Stasis distribution: histogram visualisation.

dynamic indicator, the Age Stasis, that accurately detects regions associated with high thrombosis risk by searching, at the same time, for slow flow conditions and old blood presence. Age Stasis allows us to accurately detect regions where blood clots formation is most probable. Furthermore, the cumulative distribution functions provided the possibility to make comparisons between different patients, quantifying how the advanced pathology influences the thrombosis risk.

Several future developments can be foreseen. First, it can be interesting to apply our procedure to determine boundary data (pressure, flowrates and displacement fields) to patients for which we can detect all these information also from medical images (as in 4D flow MRI). In this way, a validation process might be used to assess at which level the novel procedure is able to predict boundary data and, by carrying out numerical simulations, to investigate how accurate the numerical results are when compared with 3D time dependent velocity data.

Another interesting development would be to perform our analysis to the whole left heart, i.e. comprising also the left ventricle in the domain, to evaluate the effects of the atrial fibrillation also on ventricular flow patterns.

Finally, due to the electric nature of the fibrillatory arrhythmia, a comparison between the indicators we discussed in this paper with some electrophysiological ones could be useful. The latter can be assessed through electrophysiological simulations or, for a complete analysis of the pathology, via a coupled electromechanics-fluid dynamics atrial simulation.

### Acknowledgments

Alberto Zingaro, Luca Dede' and Alfio Quarteroni have been funded by Italian Ministry of University and Research (MIUR) within the PRIN (Research projects of relevant national interest 2017 «Modeling the heart across the scales: from cardiac cells to the whole organ» Grant Registration number 2017AXL54F)

### Appendix A. Parameter values of lumped-parameter model

In this Appendix, we report the values chosen for the parameters of the lumped-parameter circulation model.

Parameter	Value	
$R_{AR}^{SYS}$	1.00	mmHg · s/mL
$C_{AR}^{SYS}$	2.00	mL/mmHg
$L_{AR}^{SYS}$	1.00	mmHg · s <sup>2</sup> /mL
$R_{VEN}^{SYS}$	0.50	mmHg · s/mL
$C_{VEN}^{SYS}$	140.00	mL/mmHg
$L_{VEN}^{SYS}$	$5 \times 10^{-4}$	mmHg · s <sup>2</sup> /mL
$R_{AR}^{PUL}$	0.04	mmHg · s/mL
$C_{AR}^{PUL}$	15.00	mL/mmHg
$L_{AR}^{PUL}$	$5 \times 10^{-4}$	mmHg · s <sup>2</sup> /mL
$R_{VEN}^{PUL}$	0.60	mmHg · s/mL
$C_{VEN}^{PUL}$	10.00	mL/mmHg
$L_{VEN}^{PUL}$	$1 \times 10^{-4}$	mmHg · s <sup>2</sup> /mL

Table A.8: Parameter values of lumped-parameter models, common to all the cases.

Parameter	PH1	AF1	AF2	AF3
$E_{RA}^{act,max}$	0.04	0.00	0.00	0.00
$E_{RA}^{pass}$	0.06	0.60	0.60	0.80
$E_{RV}^{act,max}$	1.20	1.20	0.70	0.70
$E_{RV}^{pass}$	0.05	0.80	0.40	0.40
$E_{LA}^{act,max}$	0.20	0.00	0.00	0.00
$E_{LA}^{pass}$	0.09	0.30	0.30	0.40
$E_{LV}^{act,max}$	6.00	4.00	1.00	1.00
$E_{LV}^{pass}$	0.08	0.20	0.20	0.20

Table A.9: Elastances values in the four distinct simulations (values in mmHg/mL)

## Appendix B. Kinetic models for red blood cells

A Lagrangian approach is helpful and it is frequently used in heart haemodynamics to analyse the red blood cells motion inside LA [40, 16, 18]. The application of a kinetic theory approach allows the derivation from the particle information of some Eulerian fields, as fields of moments of the fluid age [53, 101] and the washout field [18].

The evaluation of the moments starting from an Eulerian perspective would require an additional computational cost because it would need, at each timestep, the resolution of a specific transport-diffusion PDE [18]. Moreover, the LES framework gives us the possibility to simulate the transport and diffusion of the particles using the Navier-Stokes velocity solution without the requirement of any assumption about the diffusion tensor, whose modeling would sensibly affect the final result. For these reasons, in this section we want to provide a brief derivation of the moments of the age and washout fields, used in 5.2. In Appendix B.1 we analyse the single-particle motion to support the typical assumption of considering the red blood cell as a massless particle [16] with a dimensional analysis. In Appendix B.2, we introduce the kinetic theory to derive the evolution PDEs in [53, 18], from our perspective. Finally, in Appendix B.3, we present the discretization procedure.

*Appendix B.1. Equation of motions for a single particle in a fluid*

The Lagrangian approach models the blood as a fluid represented by the plasma, filled with particles transported by the flow [54]. In particular, we focus on the red blood cells because of their high concentration (about the 45% is made of red blood cells and the 55% of plasma and the remaining particles occupy less than 1% of the total volume).

Considering the cells as single particles, for which we can neglect both the gravitational effects and the collisional interaction between themselves, the equation of motion of the  $P$ -th one can be written as follows:

$$\frac{d\mathbf{v}_P(t)}{dt} = \frac{1}{\tau_P}(\mathbf{u}(\mathbf{x}_P(t), t) - \mathbf{v}_P(t)) \quad t \in (0, T), \quad (\text{B.1})$$

where  $\tau_P$  is the particle response time in our flow regime [52, 102],  $\mathbf{u}$  is the fluid velocity field, and  $\mathbf{x}_P$  and  $\mathbf{v}_P$  are the particle position and velocity, respectively. Sure of the correctness of Equation B.1, we want to make some simplifications to reduce the problem to the resolution of an interpolation problem.

Under the Stokes flow assumption, we would have a response time  $\tau_0$  with the analytical formulation [52]:

$$\tau_0 = \frac{\rho_P d_P^2}{18\mu}, \quad (\text{B.2})$$

where  $\mu$  is the fluid dynamic viscosity,  $d_P = 7.8 \times 10^{-6}$  m is the red blood cell diameter and  $\rho_P = 1.11\text{g/mL}$  is the blood cell density. In our case we need a correction of particle response time, due to the transitional regime of the flow, which becomes the following [52]:

$$\tau_P = \frac{\tau_0}{\phi(\text{Re}_P)}, \quad (\text{B.3})$$

where  $\text{Re}_P$  is the particle Reynolds number [52], given by:

$$\text{Re}_P = \frac{d_P |\mathbf{u}(\mathbf{x}_P(t), t) - \mathbf{v}_P(t)|_2 \rho}{\mu}. \quad (\text{B.4})$$

If we compute the  $\text{Re}_P$ , using an estimate of  $|\mathbf{u}(\mathbf{x}_P(t), t) - \mathbf{v}_P(t)|_2 \simeq 10^{-4}$  m/s [103], we obtain  $\text{Re}_P \simeq 3 \cdot 10^{-4}$ .

In Equation B.3, we use the Schiller-Neumann approximation (see [104]) for  $\text{Re}_P < 10^3$ :

$$\phi(\text{Re}_P) = 1 + 0.15\text{Re}_P^{0.687}, \quad (\text{B.5})$$

then we obtain  $\phi(\text{Re}_P) \simeq 1$ . For this reason, we have the possibility to make the approximation  $\tau_P \simeq \tau_0$ . We can define the Stokes number to compare it with the flow time scale  $\tau$  as [52]:

$$\text{St} = \frac{\tau_0}{\tau} = \frac{\rho_P d_P^2 U}{\mu L}, \quad (\text{B.6})$$

where  $U$  and  $L$  are the characteristic velocity and length, respectively.

Substituting the values in Equation B.6, we can notice that  $\text{St} \ll 1$ . This value justifies the approximation of the red cells with a tracer, as in [16]. Then the particle velocity can be approximated with the value of the fluid velocity in the particle position:

$$\mathbf{v}_P(t) = \mathbf{u}(\mathbf{x}_P(t), t). \quad (\text{B.7})$$

Finally, the equation of motion of the  $P$ -th single red blood cell:

$$\begin{cases} \frac{d\mathbf{x}_P(t)}{dt} = \mathbf{v}_P(t) \\ \mathbf{v}_P(t) = \mathbf{u}(\mathbf{x}_P(t), t) \end{cases} \quad (\text{B.8})$$

### Appendix B.2. Kinetic equation for the particle distribution

The description of a large number of particles requires the introduction of a statistical approach. First of all, we consider  $N_P$  particles describing the  $j$ -th one, using the position  $\mathbf{x}_j(t)$  and velocity  $\mathbf{v}_j(t)$ . Starting from that the microscopic distribution function in the phase space can be defined as the product of two Dirac delta functions  $\delta$ :

$$f_m(\mathbf{x}, \mathbf{v}, t) = \sum_{j=1}^{N_P} \delta(\mathbf{x} - \mathbf{x}_j(t)) \delta(\mathbf{v} - \mathbf{v}_j(t)), \quad (\text{B.9})$$

where, the first  $\delta$  is a function of the spatial variable, and the second one is velocity-dependent. The distribution  $f_m$  evolves according to Liouville equation for the particle transport [52]:

$$\frac{\partial f_m}{\partial t} + \mathbf{v} \cdot \frac{\partial f_m}{\partial \mathbf{x}} + \frac{\partial}{\partial \mathbf{v}} \cdot \left( \frac{\mathbf{u} - \mathbf{v}}{\tau_P} f_m \right) = 0. \quad (\text{B.10})$$

Then we apply an ensemble average operation  $\langle \cdot \rangle$  over the random realizations of the velocity field  $\mathbf{u}$  to separate the fluctuating components of the turbulent motion (see [52]), as follows:

$$f_m = \langle f_m \rangle + \tilde{f}_m = f + \tilde{f}_m \quad \mathbf{u} = \langle \mathbf{u} \rangle + \tilde{\mathbf{u}} = \mathbf{U} + \tilde{\mathbf{u}} \quad (\text{B.11})$$

This provides the definition of  $f(\mathbf{x}, \mathbf{v}, t)$  which is the probability density for a particle to have position  $\mathbf{x}$  and velocity  $\mathbf{v}$  at instant time  $t$ . The function  $f$  evolves according to the following equation [52]:

$$\frac{\partial f}{\partial t} + \mathbf{v} \cdot \frac{\partial f}{\partial \mathbf{x}} + \frac{\partial}{\partial \mathbf{v}} \cdot \left( \frac{\mathbf{U} - \mathbf{v}}{\tau_P} f \right) = -\frac{1}{\tau_P} \frac{\partial}{\partial \mathbf{v}} \cdot \langle \tilde{\mathbf{u}} \tilde{f}_m \rangle. \quad (\text{B.12})$$

This equation can be used to detect the Eulerian equations which describe the problem from a continuous mechanics point of view. Indeed, we can define:

- the average volume concentration:

$$\Phi(\mathbf{x}, t) = \int_{\mathbb{R}^3} f(\mathbf{x}, \mathbf{v}, t) d\mathbf{v}, \quad (\text{B.13})$$

- the disperse phase's velocity:

$$\mathbf{V}(\mathbf{x}, t) = \frac{1}{\Phi(\mathbf{x}, t)} \int_{\mathbb{R}^3} \mathbf{v} f(\mathbf{x}, \mathbf{v}, t) d\mathbf{v}, \quad (\text{B.14})$$

which allows us to construct a decomposition of the particles velocity in  $\mathbf{v} = \mathbf{V} + \mathbf{v}'$ , where  $\mathbf{v}'$  is the fluctuating component [52].

In our case, following the procedure in [52] and considering  $\tau_p \rightarrow 0$  since  $St \ll 1$ , we can derive the equations:

$$\begin{cases} \mathbf{V} = \mathbf{U} - \mathbf{D} \cdot \nabla \ln(\Phi) & \text{in } \mathbb{R}^3, \\ \frac{\partial \Phi}{\partial t} + \nabla \cdot (\Phi \mathbf{U}) = \nabla \cdot (\mathbf{D} \cdot \nabla \Phi) & \text{in } \mathbb{R}^3, \end{cases} \quad (\text{B.15})$$

where  $\mathbf{D}$  is a tensor which describes the turbulent diffusion of the particles [52]. In our context, we have inflow and outflow of blood. For this reason, we define a particle distribution function  $f_\tau$  depending on the injection time of the particle  $\tau$  in the atrium.

Then the average volume concentration of the tracer injected at the time  $\tau$  is:

$$\Phi_\tau(\mathbf{x}, t, \tau) = \int_{\mathbb{R}^3} f_\tau(\mathbf{x}, \mathbf{v}, t, \tau) d\mathbf{v}. \quad (\text{B.16})$$

Following the steps we described before considering the dependence on  $\tau$  we arrive to:

$$\rho_P \frac{\partial \Phi_\tau}{\partial t} + \nabla \cdot (\rho_P \Phi_\tau \mathbf{U}) = \nabla \cdot (\rho_P \mathbf{D} \cdot \nabla \Phi_\tau) \quad (\text{B.17})$$

which is the evolution equation  $\tau$ -family of [53] for a non reactive tracer, with the only difference that  $\Phi_\tau$  is not exactly a distribution because its integral in space gives us the number of particles and not 1.

In this case, we need some minor changes in the formulation of the moment generations, using:

$$\Phi(\mathbf{x}, t) = \int_{-\infty}^t \Phi_\tau(\mathbf{x}, t, \tau) d\mathbf{x}, \quad (\text{B.18})$$

which represents the average volume concentration at time  $t$ , considering all the particles injected until that moment. This can be used in the definition of the  $k$ -th moment of the age:

$$m_k(\mathbf{x}, t) = \frac{1}{\Phi(\mathbf{x}, t)} \int_{-\infty}^t (t - \tau)^k \Phi_\tau(\mathbf{x}, t, \tau) d\tau \quad k \in \mathbb{N}, \quad (\text{B.19})$$

which can be related with an integration over  $\tau$  of the equation B.17 to the following evolution equation of the  $k$ -th moment:

$$\frac{\partial(\rho_P \Phi m_k)}{\partial t} + \nabla \cdot (\rho_P \Phi m_k \mathbf{U}) = \nabla \cdot (\rho_P \mathbf{D} \cdot \nabla (\Phi m_k)) + \rho_P \Phi k m_{k-1}, \quad (\text{B.20})$$

This is the commonly used moment generation equation [101, 53, 18]. It is interesting to notice that a common assumption made using Equation B.20 is  $m_0 = 1$ . From our procedure, this condition is automatically derived by the kinetic definition of  $m_k$ .

The idea of the separation of the function  $f$  using the continuous family of functions  $(f)_{\tau \in \mathbb{R}}$  gives us the possibility to derive the moment generation from the kinetic theoretical background arriving to a theoretically equivalent result.

Another indicator we want to connect to our Lagrangian formulation is the washout field, which can be defined as:

$$\psi_{\bar{t}}(\mathbf{x}, t) = \frac{1}{\Phi(\mathbf{x}, t)} \int_{-\infty}^t H(\bar{t} - \tau) \Phi_\tau(\mathbf{x}, t, \tau) d\tau \quad (\text{B.21})$$

where  $H$  is the Heaviside function. This parameter gives us a concentration  $\text{Im}(\psi_{\bar{t}}) = [0, 1]$  of the tracer injected after the time  $\bar{t}$  on the overall tracer concentration. In particular, when  $\psi_{\bar{t}} = 0$ , we

have high concentration of young tracer [18]. Indeed, if we consider  $t < \bar{t}$  then in the integration  $\tau < t$  for each  $\tau$  and  $\psi_{\bar{t}} = 1$ .

Then, if we multiply the equation B.17 by the Heaviside function and we integrate over  $\tau$  we have the equation:

$$\frac{\partial(\rho_P \Phi \psi_{\bar{t}})}{\partial t} + \nabla \cdot (\rho_P \Phi \psi_{\bar{t}} \mathbf{U}) = \nabla \cdot (\mathbf{D} \cdot \nabla(\rho_P \Phi \psi_{\bar{t}})) \quad (\text{B.22})$$

which is the scalar transport equation used to describe the washout.

### Appendix B.3. Numerical approximation

The particle simulation can be segregated from the NS problem, indeed we assumed that the particles do not effect the fluid motion. The simulation will be so carried out using an approximation of the particle velocity and position as follows for  $n = 0, \dots, N_\theta - 1$ :

$$\begin{cases} \mathbf{x}_p^{n+1} = \mathbf{x}_p^n + \Delta\theta \mathbf{v}_p^n \\ \mathbf{v}_p^n = \mathbf{u}(\mathbf{x}_p^n) \end{cases} \quad (\text{B.23})$$

where  $\Delta\theta = T/N_\theta$  is the time discretization step, which can be also bigger than the one we use to solve the Navier-Stokes problem, if compatible with the stability requirements of an Explicit Euler method. This approach needs an interpolation of the velocity field we computed in an Eulerian way. Indeed, the  $\mathbf{u}$  values are stored at the mesh grid points, which do not match with the particle position at any time.

The velocity numerical approximation will be the following [59]:

$$\mathbf{u} = \mathbf{u}_h + \mathbf{u}' \simeq \mathbf{u}_h - \tau_M(\mathbf{u}_h) \mathbf{r}_M(\mathbf{u}_h, p_h). \quad (\text{B.24})$$

Indeed, choosing the FEM solution  $\mathbf{u}_h$  and neglecting the turbulence component of the velocity  $\mathbf{u}'$ , the approximation on coarse meshes yields poor results than those of DNS [105], causing infinite residence times of particles near to the boundary, in analogy with the negligible turbulent diffusion in the PDEs [106].

The choice of the fine-scale component consideration in the tracking is commonly used in Lagrangian Parcels Tracking in LES framework [107, 105]. However, no results are present in literature about a Lagrangian analysis, coupled with a VMS-LES framework and in most cases, the fine-scale corrections use stochastic Brownian motion to model  $\mathbf{u}'$  [105, 108].

The approach we will use to simulate the red blood cells constructs some macro-particles, which we will call from now on parcels. This approximation, known as Discrete Parcel Method (DPM), is commonly used in many different applications [99]. Moreover, the Particle-In-Cell Method for plasma simulations [109] or the Moist-Parcel-In-Cell Method for cloud particles [110] use the same idea, and they are commonly used to recover Eulerian fields. We consider  $N_H$  parcels, and we define a weight for the simulation, which is the fraction between the number of physical particles over the number of simulated particles:

$$\omega_j = \frac{N_P}{N_H}. \quad (\text{B.25})$$

We consider a constant  $\omega = \omega_j$ ,  $\forall j = 1, \dots, N_H$ . Moreover, we assume that a single parcel  $j$  has a definite velocity, but also a spatial extension, given by a shape function  $S$ . In this way, we can approximate the distribution function as follows:

$$f_h(\mathbf{x}, \mathbf{v}, t) = \sum_{j=1}^{N_H} \omega_j S(\mathbf{x} - \mathbf{x}_j(t)) \delta(\mathbf{v} - \mathbf{v}_j(t)). \quad (\text{B.26})$$

Our choice about the function  $S$  will be a 3D extension of the cloud-in-cell described by [111]:

$$S(|\mathbf{x}|) = \frac{1}{4\pi R^3/3} \chi_{\{|\mathbf{x}| < R\}}, \quad (\text{B.27})$$

where  $R = R(h)$  is a function of the mesh element size; we will use it to compute the weight of a particle. The choice of this value needs to respect some physical constraint. First of all, we cannot consider a sphere too small to contain  $\omega_j$  particles, because we cannot overestimate the density of cells:

$$R \geq R_{\omega_j} = \sqrt[3]{\frac{3V_{\omega_j}}{4\pi}}, \quad (\text{B.28})$$

where  $V_{\omega_j}$  is the minimum volume which contains a number  $\omega_j$  of red blood cells, considering that the mean estimate is about  $5.5 \times 10^6$  cells/mm<sup>3</sup>. In our simulations, we choose the following expression of  $R$ :

$$R = h = \frac{1}{|\mathcal{T}_h|} \sum_{K \in \mathcal{T}_h} h_K, \quad (\text{B.29})$$

where  $h$  is the average mesh size.

Then, the function  $S$  has the properties of symmetry, compact support and unitary integral, which are fundamental in the derivation of motion equations, which can be proved to be the same of the real single particle, following the procedure of [111] on our equations.

The utility of this procedure is the derivation of the Eulerian fields from the Lagrangian one. Indeed, considering each parcel  $j$  entering in the domain at time  $\Theta_j$ , we can compute an approximation of the age  $K$ -th moment field at each grid node  $\mathbf{x}_i$ , as the age  $K$ -th moment average over the parcels which are distant from the point less than  $R$ :

$$m_{K,h}^n(\mathbf{x}_i) = \frac{\sum_{j=1}^{N_H} (t - \Theta_j)^K \omega_j S(\mathbf{x}_i - \mathbf{x}_j^n)}{\sum_{j=1}^{N_H} \omega_j S(\mathbf{x}_i - \mathbf{x}_j^n)} \quad (\text{B.30})$$

Finally, we can use the same calculation also to find the washout from the same perspective:

$$\psi_{i,h}^n(\mathbf{x}_i) = \frac{\sum_{j=1}^{N_H} H(\bar{t} - \Theta_j) \omega_j S(\mathbf{x}_i - \mathbf{x}_j^n)}{\sum_{j=1}^{N_H} \omega_j S(\mathbf{x}_i - \mathbf{x}_j^n)} \quad (\text{B.31})$$

## References

- [1] A. Di Carlo, L. Bellino, D. Consoli, F. Mori, A. Zaninelli, M. Baldereschi, A. Catterinussi, M. G. D'Alfonso, C. Gradia, B. Sgherzi, G. Pracucci, B. Piccardi, B. Polizzi, D. Inzitari, Prevalence of atrial fibrillation in the Italian elderly population and projections from 2020 to 2060 for Italy and the European Union: the fai project, *Eurospace 00* (2019) 1–8.
- [2] Y.-k. Iwasaki, K. Nishida, T. Kato, S. Nattel, Atrial fibrillation pathophysiology: Implications for management, *Circulation* 124 (2011) 2264–2274.
- [3] P. Kowey, G. V. Naccarelli, *Atrial Fibrillation*, 1st Edition, Marcel Dekker, 2005.
- [4] U. Schotten, S. Verheule, P. Kirchhof, A. Goette, Pathophysiological mechanisms of atrial fibrillation: A translational appraisal, *Physiological Reviews* 91 (2009) 265–325.
- [5] H. Azzam, *Atrial Fibrillation - Mechanisms and Treatment*, Intech, 2013, Ch. Thrombogenesis in Atrial Fibrillation, pp. 127–151.



- [6] A. J. Sanfilippo, V. M. Abascal, M. Sheehan, L. B. Oertel, P. Harrigan, R. A. Hughes, A. E. Weyman, Atrial enlargement as a consequence of atrial fibrillation, *Circulation* 82 (1990) 792–797.
- [7] V. P. Kamphuis, J. J. M. Westenberg, R. L. F. van del Palen, N. A. Blom, A. de Roos, R. van der Geest, M. S. M. Elbaz, A. A. W. Roest, Unravelling cardiovascular disease using four dimensional flow cardiovascular magnetic resonance, *International Journal of Cardiovascular Imaging* 33 (2017) 1069–1081.
- [8] M. Markl, M. Carr, J. Ng, D. C. Lee, K. Jarvis, J. Carr, J. J. Goldberger, Assessment of left and right atrial 3D hemodynamics in patients with atrial fibrillation: a 4D flow MRI study, *International Society for Magnetic Resonance in Medicine* 32 (2016) 807–815.
- [9] M. Markl, D. C. Lee, J. Ng, M. Carr, J. Carr, J. J. Goldberger, Left atrial 4D flow MRI: Stasis and velocity mapping in patients with atrial fibrillation, *Investigative Radiology* 51 (2016) 147–154.
- [10] J. Zimmermann, M. Loecher, F. O. Kolawole, K. Bäuml, K. Gifford, S. A. Dual, M. Levenston, A. L. Marsden, D. B. Ennis, On the impact of vessel wall stiffness on quantitative flow dynamics in a synthetic model of the thoracic aorta, *Scientific Reports* 11 (2021) 6703.
- [11] M. T. Ngo, U. Y. Lee, H. Ha, N. Jin, G. H. Chung, Y. G. Kwak, J. Jung, H. S. Kwak, Comparison of hemodynamic visualization in cerebral arteries: Can magnetic resonance imaging replace computational fluid dynamics?, *Journal of Personalized Medicine* 11 (2021) 253.
- [12] E. Ferdian, A. Suinesiaputra, D. J. Dubowitz, D. Zhao, A. Wang, B. Cowan, A. A. Young, 4dflownet: Super-resolution 4D flow MRI using deep learning and computational fluid dynamics, *Frontiers in Physics* 8 (2020) 138.
- [13] M. Cibis, K. Jarvis, M. Markl, M. Rose, C. Rigsby, A. J. Barker, J. J. Wentzel, The effect of resolution on viscous dissipation measured with 4D flow MRI in patients with Fontan circulation: Evaluation using computational fluid dynamics, *Journal of Biomechanics* 48 (12) (2015) 2984–2989.
- [14] A. Roldán-Alzate, S. García-Rodríguez, P. V. Anagnostopoulos, S. Srinivasan, O. Wieben, C. J. François, Hemodynamic study of TCPC using in vivo and in vitro 4D flow MRI and numerical simulation, *Journal of Biomechanics* 48 (7) (2015) 1325–1330.
- [15] G. Annio, R. Torii, B. Ariff, D. P. O’Regan, V. Muthurangu, A. Ducci, V. Tsang, G. Burriesci, Enhancing Magnetic Resonance Imaging With Computational Fluid Dynamics, *Journal of Engineering and Science in Medical Diagnostics and Therapy* 2 (2019) 041010.
- [16] C. Chnafa, Using image-based large-eddy simulations to investigate the intracardiac flow and its turbulent nature, Ph.D. thesis, Université Montpellier II (2014).
- [17] I. Fumagalli, M. Fedele, C. Vergara, L. Dede’, S. Ippolito, F. Nicolò, C. Antona, R. Scrofani, A. Quarteroni, An image-based computational hemodynamics study of the systolic anterior motion of the mitral valve, *Computers in Biology and Medicine* 123 (2020) 103922.
- [18] J. Dueñas-Pamplona, J. García García, J. Sierra-Pallares, C. Ferrera, R. Agujetas, J. R. López-Mínguez, A comprehensive comparison of various patient-specific CFD models of the left atrium for atrial fibrillation patients, *Computers in Biology and Medicine* 133 (2021) 104423.
- [19] E. Karabelas, S. Longobardi, J. Fuchsberger, O. Razeghi, C. Rodero, M. Strocchi, R. Rajani, G. Haase, G. Plank, S. Niederer, Global sensitivity analysis of four chamber heart hemodynamics using surrogate models (2021). [arXiv:2111.08339](https://arxiv.org/abs/2111.08339).
- [20] L. T. Zhang, M. Gay, Characterizing left atrial appendage functions in sinus rhythm and atrial fibrillation using computational models, *Journal of Biomechanics* 41 (2008) 2515–2523.
- [21] D. Vella, A. Monteleone, G. Musotto, G. M. Bosi, G. Burriesci, Effect of the alterations in contractility and morphology produced by atrial fibrillation on the thrombosis potential of the left atrial appendage, *Frontiers in Bioengineering and Biotechnology* 9 (2021) 586041.
- [22] R. Koizumi, K. Funamoto, T. Hayase, Y. Kanke, M. Shibata, Y. Shiraishi, T. Yambe, Numerical analysis of hemodynamic changes in the left atrium due to atrial fibrillation, *Journal of Biomechanics* 48 (2015) 472–478.
- [23] T. Otani, A. Al Issa, A. Pourmorteza, E. R. McVeigh, S. Wada, H. Ashikaga, A computational framework for personalized blood flow analysis in the human left atrium, *Annals of Biomedical Engineering* 44 (2016) 3284–3294.
- [24] A. Masci, M. Alessandrini, D. Forti, F. Menghini, L. Dede’, C. Tommasi, A. M. Quarteroni, C. Corsi, A patient-specific computational model of left atrium in atrial fibrillation: Development and initial evaluation, in: *Lecture Notes in Computer Science*, Vol. 10263, 2017, pp. 392–400.
- [25] A. Masci, M. Alessandrini, D. Forti, F. Menghini, L. Dede’, C. Tommasi, A. M. Quarteroni, C. Corsi, Development of a computational fluid dynamics model of the left atrium in atrial fibrillation on a patient specific basis, in: *Europace*, Vol. 19, 2017, pp. 120–121.
- [26] D. Dillon-Murphy, D. Marlevi, B. Ruijsin, A. Qureshi, H. Chubb, E. Kerfoot, M. O’Neill, D. Nordsletten, O. Aslanidi, A. de Vecchi, Modeling left atrial flow, energy, blood heating distribution in response to catheter ablation therapy, *Frontiers in Physiology* 9 (2018) 1757.
- [27] D. Forti, L. Dede’, Semi-implicit BDF time discretization of the Navier-Stokes equations with VMS-LES model-

- ing in a high performance computing framework, *Computers and Fluids* 117 (2015) 168–182.
- [28] A. Masci, L. Barone, L. Dede', M. Fedele, C. Tomasi, A. M. Quarteroni, C. Corsi, The impact of left atrium appendage morphology on stroke risk assessment in atrial fibrillation: A computational fluid dynamics study, *Frontiers in Physiology* 9 (2019) 1938.
- [29] G. García Isla, A. L. Olivares, M. Silva, Etelvino nd Nuñez-García, C. Butakoff, D. Sanchez-Quintana, H. Morales, X. Freixa, J. Noailly, T. de Potter, O. Camara, Sensitivity analysis of geometrical parameters to study haemodynamics and thrombus formation in the left atrial appendage, *Journal for Numerical Methods in Biomedical Engineering* 34 (2018) e03100.
- [30] G. M. Bosi, A. Cook, R. Rai, L. J. Menezes, S. Schievano, R. Torii, G. Burriesci, Computational fluid dynamics analysis of the left atrial appendage to predict thrombosis risk, *Frontiers in Cardiovascular Medicine* 5 (2018) 34.
- [31] Y. Wang, Y. Qiao, Y. Mao, C. Jiang, J. Fan, K. Luo, Numerical prediction of thrombosis risk in left atrium under atrial fibrillation, *Mathematical Biosciences and Engineering* 17 (2020) 2348–2360.
- [32] J. Mill, A. L. Olivares, E. Silva, I. Genua, A. Fernandez, A. Aguado, M. Nuñez-Garcia, T. de Potter, X. Freixa, O. Camara, Joint analysis of personalized in-silico haemodynamics and shape descriptors of the left atrial appendage, in: *Statistical Atlases and Computational Models of the Heart. Atrial Segmentation and LV Quantification Challenges*, Springer International Publishing, 2019, pp. 58–66.
- [33] D. Jia, B. Jeon, H.-B. Park, H.-J. Chang, L. T. Zhang, Image-based flow simulations of pre- and post-left atrial appendage closure in the left atrium, *Cardiovascular Engineering and Technology* 10 (2019) 225–241.
- [34] C. H. Roney, R. Bendikas, F. Pashakhanloo, C. Corrado, E. J. Vigmond, E. R. McVeigh, N. A. Trayanova, S. A. Niederer, Constructing a human atrial fibre atlas, *Annals of Biomedical Engineering* 49 (2021) 233–250.
- [35] C. H. Roney, R. Bendikas, F. Pashakhanloo, C. Corrado, E. J. Vigmond, E. R. McVeigh, N. A. Trayanova, S. A. Niederer, Constructing a human atrial fibre atlas (2020). doi:10.5281/zenodo.3764917. URL <https://doi.org/10.5281/zenodo.3764917>
- [36] F. Pashakhanloo, D. A. Herzka, H. Ashikaga, S. Mori, N. Gai, D. A. Bluemke, N. A. Trayanova, E. R. McVeigh, Myofiber architecture of the human atria as revealed by submillimeter diffusion tensor imaging, *Circulation Arrhythmia and Electrophysiology* 9 (2016) e004133.
- [37] D. Marlevi, B. Ruijsink, M. Balmus, D. Dillon-Murphy, D. Fovargue, K. Pushparajah, C. Bertoglio, M. Colarietti-Tosti, M. Larsson, P. Lamata, C. A. Figueroa, R. Razavi, D. A. Nordsletten, Estimation of cardiovascular relative pressure using virtual work-energy, *Scientific Reports* 9 (2019).
- [38] F. Regazzoni, M. Salvador, P. Africa, M. Fedele, L. Dede', A. Quarteroni, A cardiac electromechanics model coupled with a lumped parameters model for closed-loop blood circulation. part I: model derivation (2020). arXiv:2011.15040.
- [39] S. Scarsoglio, A. Guala, C. Camporeale, L. Ridolfi, Impact of atrial fibrillation on the cardiovascular system through a lumped-parameter approach, *Medical and Biological Engineering and Computing* 52 (2014) 905–920.
- [40] A. Zingaro, L. Dede', F. Menghini, A. Quarteroni, Hemodynamics of the heart's left atrium based on a variational multiscale-LES numerical model, *European Journal of Mechanics - B/Fluids* 89 (2021) 380–400.
- [41] A. Zingaro, I. Fumagalli, L. Dede', M. Fedele, P. C. Africa, A. F. Corno, A. M. Quarteroni, A geometric multiscale model for the numerical simulation of blood flow in the human left heart (2021). arXiv:2110.02114.
- [42] A. Tagliabue, L. Dede', A. M. Quarteroni, Complex blood flow patterns in an idealized left ventricle: A numerical study, *Chaos: An Interdisciplinary Journal of Nonlinear Science* 27 (2017) 093939.
- [43] A. Tagliabue, L. Dede', A. M. Quarteroni, Fluid dynamics of an idealized left ventricle: the extended Nitsche's method for the treatment of heart valves as mixed time varying boundary conditions, *International Journal for Numerical Methods in Fluids* 84 (2017) 135–164.
- [44] L. Dede', F. Menghini, A. Quarteroni, Computational fluid dynamics of blood flow in an idealized left human heart, *International Journal for Numerical Methods in Biomedical Engineering* 37 (2021) 1–26.
- [45] B. Baccani, F. Domenichini, G. Pedrizzetti, Vortex dynamics in a model left ventricle during filling, *European Journal of Mechanics - B/Fluids* 21 (2002) 527–543.
- [46] F. Domenichini, G. Pedrizzetti, B. Baccani, Three-dimensional filling flow into a model left ventricle, *Journal of Fluid Mechanics* 539 (2005) 179–198.
- [47] X. Zheng, J. Seo, V. Vedula, T. Abraham, R. Mittal, Computational modeling and analysis of intracardiac flows in simple models of the left ventricle, *European Journal of Mechanics - B/Fluids* 35 (2012) 31–39.
- [48] J. H. Seo, R. Mittal, Effect of diastolic flow patterns on the function of the left ventricle, *Physics of Fluids* 25 (2013) 110801.
- [49] L. Gan, L. Yu, M. Xie, W. Feng, J. Yin, Analysis of real-time three dimensional transesophageal echocardiography in the assessment of left atrial appendage function in patients with atrial fibrillation, *Experimental and Therapeutic Medicine* 12 (2016) 3323–3327.
- [50] M. Fedele, E. Faggiano, L. Dede', A. Quarteroni, A patient-specific aortic valve model based on moving resistive immersed implicit surfaces, *Biomechanics and Modeling in Mechanobiology* 16 (2017) 1779–1803.
- [51] L. Feng, H. Gao, B. Griffith, S. Niederer, X. Luo, Analysis of a coupled fluid-structure interaction model of the left

- atrium and mitral valve, *International Journal for Numerical Methods in Biomedical Engineering* 35 (11) (2019) e3254.
- [52] L. Zaichik, V. M. Alipchenkov, E. G. Sinaiski, *Particles in Turbulent Flows*, 1st Edition, Wiley-Vch, 2008.
- [53] J. Sierra-Pallares, C. Méndez, P. García-Carrascal, F. Castro, Spatial distribution of mean age and higher moments of unsteady and reactive tracers: Reconstruction of residence time distributions, *Applied Mathematical Modelling* 46 (2017) 312–327.
- [54] A. Quarteroni, L. Dede', A. Manzoni, C. Vergara, *Mathematical Modelling of the Human Cardiovascular System: Data, Numerical Approximation, Clinical Applications*, 1st Edition, Cambridge University Press, 2019.
- [55] J. A. Vierendeels, K. Riemsdagh, E. Dick, P. R. Verdonck, Computer simulation of intraventricular flow and pressure gradients during diastole, *Journal of Biomechanical Engineering* 122 (2000) 667–674.
- [56] A. Quarteroni, A. Manzoni, C. Vergara, The cardiovascular system: mathematical modeling, numerical algorithms, clinical applications, *Acta Numerica* 26 (2017) 365–590.
- [57] J. Donea, S. Giuliani, J.-P. Halleux, An arbitrary Lagrangian-Eulerian finite element method for transient dynamics fluid-structure interactions, *Computer Methods in Applied Mechanics and Engineering* 33 (1982) 689–723.
- [58] C. Bertoglio, A. Caiazzo, Y. Bazilevs, M. Braack, M. Esmaily, V. Gravemeier, A. Marsden, O. Pironneau, I. Vignon-Clementel, W. A. Wall, Benchmark problems for numerical treatment of backflow at open boundaries, *International Journal for Numerical Methods in Biomedical Engineering* 34 (2017) e2918.
- [59] Y. Bazilevs, V. M. Calo, J. A. Cottrell, T. J. R. Hughes, A. Reali, G. Scovazzi, Variational multiscale residual-based turbulence modeling for large eddy simulation of incompressible flows, *Computer Methods in Applied Mechanics and Engineering* 197 (2007) 173–201.
- [60] A. Quarteroni, A. Veneziani, C. Vergara, Geometric multiscale modeling of the cardiovascular system, between theory and practice, *Computer Methods in Applied Mechanics and Engineering* 302 (2016) 193–252.
- [61] K. M. Olsson, N. P. Nickel, J. Tongers, M. M. Hoeper, Atrial flutter and fibrillation in patients with pulmonary hypertension, *International Journal of Cardiology* 167 (2013) 2300–2305.
- [62] O. Yousefian, S. Carlson, A. Keibel, R. Doshi, L. Saxon, Effect of atrial fibrillation on pulmonary artery pressures in ambulatory heart failure patients, *Journal of Cardiac Failure* 23 (2017) S61.
- [63] H. T. Dodge, F. T. Kirkham, C. V. King, Ventricular dynamics in atrial fibrillation, *Circulation* 15 (1957) 335–347.
- [64] P. Alboni, S. Scarfò, G. Fucà, N. Paparella, P. Yannacopulu, Hemodynamics of idiopathic paroxysmal atrial fibrillation, *Pacing and Clinical Electrophysiology* 18 (1995) 980–985.
- [65] P. K. Kundu, I. M. Cohen, D. R. Dowling, G. Tryggvason, *Fluid Mechanics*, 6th Edition, Academic Press, 2015.
- [66] N. M. Al-Saady, O. A. Obel, A. J. Camm, Left atrial appendage: Structure, function, and role in thromboembolism, *Heart* 82 (1999) 547–554.
- [67] G. Ernst, C. Stöllberger, F. Abzieher, W. Veit-Dirscherl, E. Bonner, B. Bibus, B. Schneider, J. Slany, Morphology of the left atrial appendage, *The Anatomical Record* 242 (1995) 553–561.
- [68] N. Y. Tan, O. Z. Yasin, A. Sugrue, A. El Sabbagh, T. A. Foley, S. J. Asirvatham, Anatomy and physiologic roles of left atrial appendage: Implications for endocardial and epicardial device closure, *Interventional Cardiology Clinics* 7 (2018) 185–199.
- [69] A. Bonito, A. Demlow, R. H. Nochetto, Finite element methods for the Laplace–Beltrami operator, in: *Geometric Partial Differential Equations - Part I*, Vol. 21, Elsevier, 2020, pp. 1–103.
- [70] C. P. Appleton, J. M. Galloway, M. S. Gonzalez, M. Gaballa, M. A. Basnight, Estimation of left ventricular filling pressures using two-dimensional and doppler echocardiography in adult patients with cardiac disease: Additional value of analyzing left atrial size, left atrial ejection fraction and the difference in duration of pulmonary venous and mitral flow velocity at atrial contraction, *Journal of the American College of Cardiology* 22 (1993) 1972–1982.
- [71] R. Kaufmann, R. Rezar, B. Strohmer, B. Wernly, M. Lichtenauer, W. Hitzl, M. Meissnitzer, K. Hergan, M. Granitz, Left atrial ejection fraction assessed by prior cardiac ct predicts recurrence of atrial fibrillation after pulmonary vein isolation, *Journal of Clinical Medicine* 10 (2021) 1–12.
- [72] P. Pellicori, E. Lukaschuk, A. Joseph, C. V. Bourantas, N. Sherwi, P. H. Loh, A. Rigby, J. Zhang, A. L. Clark, J. G. F. Cleland, Clinical significance of left atrial ejection fraction measured by MRI in patients with suspected heart failure, *European Heart Journal* 34 (2013) P1492.
- [73] T. Heldt, E. B. Shim, R. D. Kamm, R. G. Mark, Computational modeling of cardiovascular response to orthostatic stress, *Journal of Applied Physiology* 92 (2002) 1239–1254.
- [74] F. Regazzoni, M. Salvador, P. Africa, M. Fedele, L. Dede', A. Quarteroni, A cardiac electromechanics model coupled with a lumped parameters model for closed-loop blood circulation. part II: numerical approximation (2020). [arXiv:2011.15051](https://arxiv.org/abs/2011.15051).
- [75] F. Liang, H. Liu, A closed-loop lumped parameter computational model for human cardiovascular system, *JSME International Journal Series C* 48 (2005) 484–493.
- [76] S. Standring, *Gray's Anatomy*, 41st Edition, Elsevier, 2016.
- [77] J. Beaudoin, J. P. Dal-Bianco, E. Aikawa, J. Bischoff, J. L. Guerrero, S. Sullivan, P. E. Bartko, M. D. Hand-

- scumacher, D.-H. Kim, J. Wylie-Sears, J. Aaron, R. A. Levine, Mitral leaflet changes following myocardial infarction: Clinical evidence for maladaptive valvular remodeling, *Circulation: Cardiovascular Imaging* 10 (2017) e006512.
- [78] A. G. Tsakiris, D. A. Gordon, R. Padiyar, D. Fréchette, Relation of mitral valve opening and closure to left atrial and ventricular pressure in the intact dog, *American Journal of Physiology* 234 (1978) H146–H151.
- [79] A. Šmalcelj, D. G. Gibson, Relation between mitral valve closure and early systolic function of the left ventricle, *Heart* 53 (1985) 436–442.
- [80] A. This, L. Boilevin-Kayl, M. A. Fernández, J.-F. Gerbeau, Augmented resistive immersed surfaces valve model for the simulation of cardiac hemodynamics with isovolumetric phases, *International Journal for Numerical Methods in Biomedical Engineering* 36 (3) (2020) e3223.
- [81] Z. M. G. Inc., Zygote solid 3D heart generation ii development report, Technical Report (2014).
- [82] M. Corti, Effects of atrial fibrillation on left atrium haemodynamics: a patient-specific computational fluid dynamics study, Master’s thesis, Politecnico di Milano (2020).
- [83] L. Antiga, M. Piccinelli, L. Botti, B. Ene-Iordache, A. Remuzzi, D. A. Steinman, An image-based modeling framework for patient-specific computational hemodynamics, *Medical and Biological Engineering and Computing* 46 (2008) 1097–1112.
- [84] Tethex repository (2021).  
URL <https://github.com/martemyev/tethex>
- [85] S. Deparis, G. Grandperrin, A. Quarteroni, Parallel preconditioners for the unsteady Navier–Stokes equations and applications to hemodynamics simulations, *Computers and Fluids* 92 (2014).
- [86] Trilinos repository (2021).  
URL <https://trilinos.github.io>
- [87] Lifex repository (2021).  
URL <https://lifex.gitlab.io/>
- [88] D. Arndt, W. Bangerth, B. Blais, M. Fehling, R. Gassmüller, T. Heister, L. Heltai, U. Köcher, M. Kronbichler, M. Maier, P. Munch, J.-P. Pelteret, S. Proell, K. Simon, B. Turcksin, D. Wells, J. Zhang, The deal.ii library, version 9.3, *Journal of Numerical Mathematics* 29 (2021).
- [89] J. Garcia, H. Sheitt, M. S. Bristow, C. Lydell, A. G. Howarth, B. Heydari, F. S. Prato, M. Drangova, R. E. Thornhill, P. Nery, S. B. Wilton, A. Skanes, J. A. White, Left atrial vortex size and velocity distributions by 4D flow MRI in patients with paroxysmal atrial fibrillation: Associations with age and CHA2DS2-VASc risk score, *International Society for Magnetic Resonance in Medicine* 51 (2019) 871–884.
- [90] M.-N. Kim, S.-M. Park, H.-D. Kim, D.-H. Cho, J. Shim, J.-i. Choi, Y. H. Kim, W. J. Shim, Assessment of the left ventricular diastolic function and its association with the left atrial pressure in patients with atrial fibrillation, *International Journal of Heart Failure* 2 (2020) 55–65.
- [91] L. Thomas, E. Foster, N. B. Schiller, Peak mitral inflow velocity predicts mitral regurgitation severity, *Journal of the American College of Cardiology* 31 (1998) 174–179.
- [92] S. F. Nagueh, O. A. Smiseth, C. P. Appleton, B. F. Byrd, H. Dokainish, T. Edvardsen, F. A. Flachskampf, T. C. Gillebert, A. L. Klein, P. Lancellotti, P. Marino, J. K. Oh, B. A. Popescu, A. D. Waggoner, Recommendations for the evaluation of left ventricular diastolic function by echocardiography: An update from the american society of echocardiography and the european association of cardiovascular imaging, *Journal of the American Society of Echocardiography* 29 (2016) 277–314.
- [93] M. Markl, D. C. Lee, N. Furiasse, M. Carr, C. Foucar, J. Ng, J. Carr, J. J. Goldberger, Left atrial and left atrial appendage 4D blood flow dynamics in atrial fibrillation, *Circulation, Cardiovascular Imaging* 9 (2016) e004984.
- [94] R. L. K. Virchow, *Archiv fuer pathologische Anatomie und Physiologie und fuer klinische Medizin*, Springer-Verlag Berlin Heidelberg, 1849.
- [95] M. Spartera, G. Pessoa Amorim, A. Stracquadanio, A. Von Ende, A. Fletcher, P. Manley, S. Neubauer, V. M. Ferreira, B. Casadei, A. T. Hess, R. S. Wijesurendra, Left atrial 4D flow cardiovascular magnetic resonance: a reproducibility study in sinus rhythm and atrial fibrillation, *Journal of Cardiovascular Magnetic Resonance* 23 (2021) 29.
- [96] D. N. Ku, D. P. Giddens, C. K. Zarins, S. Glagov, Pulsatile flow and atherosclerosis in the human carotid bifurcation. positive correlation between plaque location and low oscillating shear stress, *Arteriosclerosis, Thrombosis, and Vascular Biology* 5 (1985) 293–302.
- [97] P. Di Achille, G. Tellides, C. A. Figueroa, J. D. Humphrey, A haemodynamic predictor of intraluminal thrombus formation in abdominal aortic aneurysms, *Proceedings of the Royal Society A: Mathematical, Physical and Engineering Sciences* 470 (2014) 20140163.
- [98] X. Morales, J. Mill, K. A. Juhl, A. Olivares, G. Jimenez-Perez, R. R. Paulsen, O. Camara, STACOM2019 - Statistical Atlases and Computational Models of the Heart. Multi-Sequence CMR Segmentation, CRT-EPiggy and LV Full Quantification Challenges, Springer, 2019, Ch. Deep Learning Surrogate of Computational Fluid Dynamics for Thrombus Formation Risk in the Left Atrial Appendage, pp. 157–166.

- [99] C. T. Crowe, J. D. Schwarzkopf, M. Sommerfeld, Y. Tsuji, *Multiphase Flows with Droplets and Particles*, 2nd Edition, CRC Press, 2021.
- [100] L. Dean, *Blood groups and red cell antigens* (2005).  
URL <https://www.ncbi.nlm.nih.gov/books/NBK2261/>
- [101] D. B. Spalding, A note on mean residence-times in steady flows of arbitrary complexity, *Chemical Engineering Science* 9 (1958) 74–77.
- [102] T. M. Burton, J. K. Eaton, Fully resolved simulations of particle turbulence interaction, *Journal of Fluid Mechanics* 545 (2005) 67–111.
- [103] Y. Sugii, R. Okuda, K. Okamoto, H. Madarame, Velocity measurement of both red blood cells and plasma of in vitro blood flow using high-speed micro PIV technique, *Measurement Science and Technology* 16 (5) (2005) 1126–1130.
- [104] R. Clift, J. Grace, M. E. Weber, *Bubbles, Drops and Particles*, 1st Edition, Dover Publications, Inc., 1975.
- [105] S. Chibbaro, C. Marchioli, M. V. Salvetti, A. Soldati, Particle tracking in LES flow fields: conditional lagrangian statistics of filtering error, *Journal of Atmospheric Sciences* 15 (2014) 22–33.
- [106] M. Liu, J. Tilton, Spatial distributions of mean age and higher moments in steady continuous flows, *AIChE Journal* 56 (2010) 2561–2572.
- [107] T. Yamaguchi, D. A. Randall, Cooling of entrained parcels in a large-eddy simulation, *Journal of Atmospheric Sciences* 69 (2012) 1118–1136.
- [108] D. G. Huilier, An overview of the lagrangian dispersion modeling of heavy particles in homogeneous isotropic turbulence and considerations on related LES simulations, *Fluids* 6 (2021) 145.
- [109] H. Fehske, R. Schneider, A. Weiße, *Computational Many-Particle Physics*, 739th Edition, Springer, 2008.
- [110] D. G. Dritschel, S. J. Böing, D. J. Parker, A. M. Blyth, The moist parcel-in-cell method for modelling moist convection, *Quarterly Journal of the Royal Meteorological Society* 144 (2018) 1695–1718.
- [111] G. Lapenta, Kinetic plasma simulation: Particle in cell method, in: *XII Carolus Magnus Summer School on Plasma and Fusion Energy Physics*, 2015, pp. 1–10.